Article

Dynamics Modeling and Suspension Parameters Optimization of Vehicle System Based on Reduced Multibody System Transfer Matrix Method

Shaoheng Hu [1,2], Xiaoting Rui [1,2,*], Junjie Gu [1,2] and Xizhe Zhang [1,2]

[1] Institute of Launch Dynamics, Nanjing University of Science and Technology, Nanjing 210094, China; hushaoheng@njust.edu.cn (S.H.); jjgu@foxmail.com (J.G.); xzzhang@njust.edu.cn (X.Z.)

[2] National Key Laboratory of Complex Multibody System Dynamics, Nanjing 210094, China

* Correspondence: ruixt@163.net

Abstract: This study introduces an innovative vehicle-modeling framework based on the Reduced Multibody System Transfer Matrix Method, incorporating wheel–ground contact and friction to analyze dynamic performance metrics, including vertical acceleration, suspension deflection, and angular acceleration. The model is applied to simulate vehicle behavior at 40 km/h on Class D road conditions. To enhance dynamic characteristics, suspension parameters were optimized using the NSGA-II algorithm. The optimization process achieved significant reductions in vertical acceleration (24.12%), suspension deflection (25.98%), and angular acceleration (4.93%). The Pareto frontier facilitated the selection of a representative solution that balances smoothness, stability, and suspension performance. Frequency, PSD, and RMS analyses were performed under different road conditions and speeds to verify the robustness of the optimization results. The application of the transfer matrix method is extended to vehicle suspension modeling and optimization, offering valuable insights into improving ride comfort and stability. Additionally, it highlights the effectiveness of advanced multi-objective optimization techniques in improving vehicle dynamics and provides a robust methodology for practical applications.

Keywords: vehicle dynamics; transfer matrix method; NSGA-II; suspension optimization

1. Introduction

The automotive industry is currently undergoing a period of transformation, primarily driven by digitalization, the principles of a circular economy, and sustainable development goals. Additionally, manufacturers are striving to address these challenges in an intensely competitive and rapidly evolving market environment. Against this backdrop, the intelligent manufacturing of the automotive sector has seen rapid development in recent years, facilitated by the application of CAE software [1]. This approach aims to evaluate the dynamic behavior of vehicles during the design, development, and prototyping phases. Compared to traditional experimental procedures, it helps reduce costs, shorten design and production timelines, and simultaneously maximize vehicle performance, comfort, environmental characteristics, quality, and safety.

The suspension system has consistently been a focal area of research within the field of vehicle dynamics. Comprising a set of rigid bodies capable of relative motion, the suspension system plays a crucial role in handling performance, stability, and comfort [2]. The function of a suspension system is to maximize the friction between the tires and the road surface, provide good steering stability, and ensure passenger comfort. Despite

the evolution throughout history, vehicle suspension systems can be divided into three categories: passive, semi-active, and active [3]. Passive suspension systems typically include springs for absorbing shock and dampers for dissipating energy and controlling the movement of the springs. More modern suspensions can also rely on external active or semi-active control mechanisms to improve grip and ride comfort. Semi-active suspension can change suspension parameters in real time, such as the damping coefficient of the shock absorber [4]. The active suspension system can adjust the vertical motion of the vehicle through the active suspension force [5]. Liang et al. [6] proposed a decentralized cooperative control framework to achieve the integration of an active front steering system and active suspension system by applying a multi-constrained distributed model predictive control approach, which aims to improve the vehicle lateral stability, ride comfort, and roll safety during path tracking. Azmi et al. [7] proposed an optimal control strategy for the energy-regenerative active suspension system based on the electromagnetic structure. Shaqarin and Noack et al.[8] proposed a safety critical controller, which is the control Lyapunov function-control barrier function-quadratic programming. Feng et al. [9] integrated the torque vectoring and active suspension system to enhance the vehicle's longitudinal and vertical motion control performance. These studies show that some state variables, such as vertical displacements and velocities of sprung and unsprung masses, are generally viewed as easy to measure. However, this assumption is not realistic in practical applications, as it is neither economical nor feasible to equip such an advanced and expensive sensor system for large-scale production vehicles [10]. The main disadvantages of semi-active versus active suspensions are their complexity, manufacturing, and maintenance costs, and associated customer service expenses [11]. Passive suspension is still the most widely used vehicle suspension system because of its low cost, high reliability, easy maintenance, and modification [12]. Numerous efforts have been undertaken to develop optimal solutions for passive suspension systems, with the literature extensively exploring various methods for designing suspension systems. Gobbi et al. [13] used a two-degree-of-freedom linear model to describe the dynamic behavior of vehicles driving on a road with random profiles. Lenka et al. [14] applied the multi-objective optimization of SUV ride comfort by MSC.ADAMS and Mode Frontier to improve the ride performance of SUVs by keeping the handling performance attributes of SUVs the same or better than the base vehicles. Su et al. [15] analyzed and optimized the motion characteristics of the McPherson suspension system of a minivan, obtained better wheel positioning parameters, and improved the performance of the suspension system. Ebrahimi-Nejad et al. [16] derived the vibration governing equation of a two-degree-of-freedom suspension system using the Lagrange equation and carried out multi-objective optimization of the maximum acceleration and displacement of unsprung and unsprung mass according to TOPSIS method. Issa and Samn [17] used the Harris Hawk Optimization algorithm to optimize the design of passive vehicle suspension systems for quarter-vehicle models and half-vehicle models.

Suspension is usually considered to be a multibody system, and the multibody dynamics analysis method is widely used in vehicle system dynamics research. A multibody system consists of various body elements and joint elements connected in arbitrary configurations. Since the 1960s, significant progress has been made in multibody system dynamics, leading to the proposal of numerous methodologies [18,19]. Despite differences in form, all these methods require the construction of global dynamic equations incorporating the inertia matrix of the system.

The advantage of the Multibody System Transfer Matrix Method (MSTMM) lies in its ability to avoid constructing global dynamic equations for the system and its use of low-order matrices independent of system degrees of freedom, enabling fast and accurate computations. In 1993, Rui et al. [20] extended the classical transfer matrix method [21],

originally developed for analyzing vibrations of one-dimensional, linear time-invariant elastic component systems, to the vibration analysis of linear rigid-flexible coupled multibody systems. For general nonlinear multibody systems, the combination of MSTMM with numerical integration programs led to the development of the Discrete-Time Multibody System Transfer Matrix Method. However, this method relies on the conditionally stable Newmark-β numerical integration approach for linearization, which only achieves second-order accuracy. While higher-order numerical integration methods can be applied, their derivation is exceedingly complex. To avoid this limitation, a new version of MSTMM (NV-MSTMM) [22] was introduced. Using acceleration as the state vector instead of displacement, NV-MSTMM simplifies solving nonlinear multibody systems. For large-scale systems, however, error accumulation during the successive multiplication of numerous transfer matrices can lead to numerical instability. To enhance numerical stability and computational accuracy, the Reduced Multibody System Transfer Matrix Method (RMSTMM) [23] was developed. This method divides the total state vector into two parts, translational and angular accelerations, and internal forces and moments, effectively halving the matrix size. As a result, RMSTMM not only retains the advantages of NV-MSTMM but also significantly improves numerical stability. MSTMM is widely used in mechanical system dynamics analysis, such as rotary blade systems, robots, buffering adsorption systems, etc., and has been applied in different types of vehicles. Chen et al. [24] investigated a coupling system of the rotating bending-torsional blade with the stator using MSTMM. By analyzing the vibration characteristics under different rotational speeds, their study highlighted the significant influence of blade rotation on system dynamics. Si et al. [25] applied the linear MSTMM to establish a vibration model for a 3-prismatic-revolute-revolute planar parallel manipulator and further explored its dynamic characteristics, providing insights into its operational performance under various conditions. Chen et al. [26] proposed a novel dynamic modeling approach based on MSTMM to analyze the impact response of a rescue robot with two flexible manipulators. Their work demonstrated the effectiveness of the method in capturing complex interactions in robotic systems. Li et al. [27] developed a method for dynamic parameter identification of an industrial robot using MSTMM. Their model accurately described dynamic characteristics, identified frequency response functions, and introduced a new dynamic parameter identification method, contributing to improved precision in industrial applications. Miao et al. [28] examined the impact dynamics and collision behavior of flexible buffering adsorption mechanisms on thin-walled plates under low-speed conditions in microgravity environments. By applying the transfer matrix method to a multirobot system, they proposed a coupled multibody dynamic model for the system and a dedicated subsystem for thin-walled plates, providing valuable insights into dynamic responses in specialized environments. Miao et al. [29] utilized RMSTMM to establish a dynamic model of the tracked system, treating the track as a long-chain system, which simplified the modeling process. Wu et al. [30] applied MSTMM to establish the dynamics model of the wheeled launch system to study its vibration characteristics. The dynamic response of the wheeled launch system under random excitation was obtained without considering large motions.

Vehicle system parameters often need to be optimized to cope with various complex working conditions. A multi-objective evolutionary method is a commonly used optimization algorithm. Deb et al. [31] developed one of the most significant variants of genetic algorithms, known as the Nondominated Sorting Genetic Algorithm II (NSGA-II). This multi-objective metaheuristic optimization algorithm utilizes the concepts of dominance and elitism to achieve a nondominated or Pareto-optimal front. Gadhvi et al. [32] conducted a comparative study on the multi-objective optimization of a half-car model's passive suspension using three major evolutionary algorithms: NSGA-II, Strength Pareto

Evolutionary Algorithm 2 (SPEA2), and Pareto Envelope-based Selection Algorithm II (PESA-II). Their results demonstrated that all three algorithms exhibited roughly similar performance. However, they observed that NSGA-II performed better in minimizing the objective vector, while SPEA2 and PESA-II tended to produce more diverse Pareto-optimal fronts. NSGA-II was also the algorithm chosen by Nagarkar et al. [33] for obtaining Pareto-optimal fronts related to the multi-objective optimization of passive suspension systems in a quarter-car model and a half-car model, respectively. Fossati et al. [34] proposed a multi-objective optimization method for the passive suspension system of a full vehicle model traveling on a random road profile. This method combines the NSGA-II algorithm and the time-domain vertical dynamic analysis of an eight-degree-of-freedom vehicle model with a seat to generate a Pareto-optimal front.

This study presents an innovative vehicle-modeling methodology utilizing the RM-STMM, offering a more comprehensive depiction of dynamic interactions than conventional approaches. The main contributions of this paper are as follows:

- A new vehicle-modeling framework is introduced based on RMSTMM that seamlessly incorporates wheel–ground contact and friction. By capturing the complex dynamic interactions between the tires and road surface, the proposed model enables more accurate evaluations of key performance metrics, such as vertical acceleration, suspension deflection, and pitch angular acceleration, under realistic road conditions.

- A multi-objective optimization strategy using the NSGA-II algorithm is developed to refine suspension parameters systematically. Results demonstrate significant reductions in vertical acceleration, suspension deflection, and pitch angular acceleration, highlighting the effectiveness of the proposed method in improving both ride comfort and handling stability. The Pareto frontier approach aids in selecting a balanced solution that meets diverse performance requirements, providing a flexible tool for suspension system design.

- A robust and scalable methodology for enhancing vehicle dynamics is illustrated. It integrates RMSTMM with advanced multi-objective optimization, extending the use of the transfer matrix method to practical engineering problems. Such an approach can be readily adapted for further research on next-generation suspension systems and other complex vehicle dynamics analyses.

The logical structure of the paper is shown in Figure 1. The paper is organized as follows: Section 2 introduces the vehicle-modeling framework using RMSTMM, including the transfer equations of body elements and joint elements of the system. Section 3 details the road modeling approach, focusing on the contact, friction, and unevenness characteristics of a Class D road surface. The dynamic simulation results, presented in Section 4, analyze the response of the vehicle under specified conditions. Section 5 employs the NSGA-II algorithm for multi-objective optimization of suspension stiffness and damping parameters, discussing the trade-offs and Pareto-optimal solutions for suspension performance. The results provide valuable insights into improving vehicle comfort and stability through parameter optimization. Section 6 discusses the advantages of combining RMSTMM and multi-objective optimization in improving vehicle dynamics and performance, also points out the limitations of current modeling and optimization frameworks, and identifies opportunities for future research to address these challenges. The conclusions are summarized in Section 7.
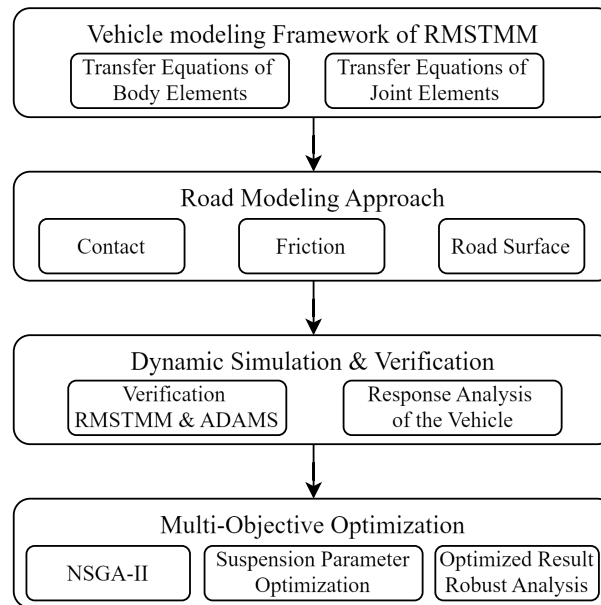
Figure 1. Logical framework of the study. The framework begins with the vehicle-modeling approach based on RMSTMM, including transfer equations for body and joint elements. This is followed by road modeling, encompassing contact, friction, and road surface characteristics. Dynamic simulation and verification steps compare RMSTMM and ADAMS results, assessing the response of the vehicle to various conditions. Finally, multi-objective optimization using NSGA-II is employed to optimize suspension parameters, with robust analysis of the optimized results.

2. Dynamics Modeling of Vehicle System

A four-wheeled vehicle with front and rear independent suspension design is studied. In addition to providing high ride quality, the suspension system should be designed to approach ideal attributes to achieve responsive handling, provide high lateral acceleration, and reduce body roll tendencies. The vehicle suspension system in real life is shown in Figure 2. A combination of harder components and more robust spring and shock absorber tuning provides better responsiveness, stability, control, and better driver feedback. On rough surfaces, the car may experience pitch, bounce, and roll motions.

Figure 2. A real-life suspension system illustrating key components, including the spring, damper, unsprung mass, and wheel assembly.

2.1. Wheeled Vehicle Dynamics Model and Topology

The dynamics model of the multibody system is established for the entire vehicle, as is shown in Figure 3. In this spatial multibody system model with large motion, the vehicle

body is considered to be a rigid body. The sprung mass of the vehicle consists of the body and its components, connected to the axles and wheels through dampers and suspension springs. The wheels and axles constitute the unsprung mass. The wheels are supported on an uneven road surface by tires with certain stiffness and damping.
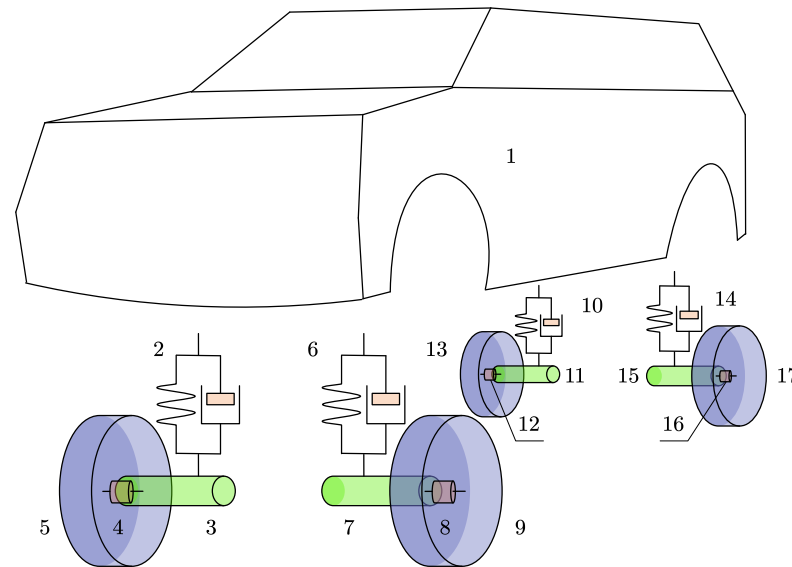
Figure 3. Schematic representation of the entire vehicle model, highlighting key components and their interactions. The model includes the vehicle body (1), suspension systems (2, 6, 10, 14), unsprung masses (3, 7, 11, 15), connections of wheel and axle (4, 8, 12, 16), and wheels (5, 9, 13, 17).

The vehicle components are numbered in sequence. Based on the natural properties of the major components of the vehicle system, RMSTMM is applied to classify them into two main categories: body elements and joint elements, which are uniformly numbered. For ease of expression, the number of dynamic elements is the same as the number of components. The corresponding relationships of dynamics model elements and vehicle components are shown in Table 1.

Table 1. The number of each vehicle component in the topology.

Component	RMSTMM	Number
Vehicle Body	Rigid body	1
Spring & Damper	Translational joint	2, 6, 10, 14
Unsprung Mass (excluding wheels)	Rigid body	3, 7, 11, 15
Connection of wheel & axle	Revolute joint	4, 8, 12, 16
Wheels	Rigid body	5, 9, 13, 17

The dynamic model topology diagram is established based on the vehicle multibody system dynamics model, as is shown in Figure 4. The graphic ◯ and □ represents the body element, and the number is the label of the body element; The arrow ⟶ indicates the joint element, the number next to it indicates the number of the joint element, and the arrow points to the transfer direction of the system state vector. The ground is marked as a rigid body 0. The four wheels 5, 9, 13, 17 and four unsprung masses 3, 7, 11, 15 are single-tip, single-root spatial motion rigid bodies, while the vehicle body 1 is a multi-tip, single-root spatial motion rigid body. The interaction between the wheel and axle is equivalent to a revolute joint 4, 8, 12, 16, and the interaction between the unsprung mass and vehicle body is equivalent to a translational joint 2, 6, 10, 14. The generalized coordinates of the system are composed of the generalized coordinates of all joint elements in the system.
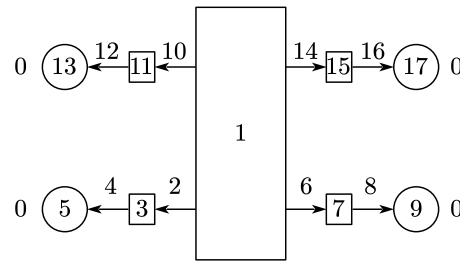
Figure 4. The dynamics model topology diagram of the entire car. Each component corresponds to the body element and joint element number as shown in Table 1.

2.2. Transfer Equation of the Vehicle

RMSTMM represents multibody systems using body elements, joint elements, and intermediate connection markers. For multi-rigid body systems, the relative motion between the root and tip markers of a joint element serves as generalized coordinates of the system. Body and joint elements are interconnected via their root (R) and tip (T) markers. State vector z of each connection marker consists of acceleration a and internal force f. Here, a encompasses translational and rotational accelerations, while f includes internal forces and moments. The state vector of a connection marker P is represented by the equation:

$$z_P = \begin{bmatrix} a_P^T & f_P^T \end{bmatrix}^T = \begin{bmatrix} \left(A_{OP}^T \ddot{r}_{OP} \right)^T & \dot{\omega}_{OP}^T & q_P^T & m_P^T \end{bmatrix}^T, \tag{1}$$

where O denotes the origin of the global inertial coordinate system $Oxyz$. The direction cosine matrix A_{OP} converts coordinates from the body-fixed coordinate system of marker P to the global inertial system. The orientation of the connected system with respect to the inertial system can be obtained by three simultaneous rotations in space and time of the three perpendicular axes with respect to the inertial system. The angles of the three rotations are θ_1, θ_2, and θ_3, respectively, and the coordinate transformation matrix of the connected system to the inertial system is [22]:

$$A = \begin{bmatrix} \cos\theta_2\cos\theta_3 & \sin\theta_1\sin\theta_2\cos\theta_3 - \cos\theta_1\sin\theta_3 & \cos\theta_1\sin\theta_2\cos\theta_3 + \sin\theta_1\sin\theta_3 \\ \cos\theta_2\sin\theta_3 & \sin\theta_1\sin\theta_2\sin\theta_3 + \cos\theta_1\cos\theta_3 & \cos\theta_1\sin\theta_2\sin\theta_3 - \sin\theta_1\cos\theta_3 \\ -\sin\theta_2 & \sin\theta_1\cos\theta_2 & \cos\theta_1\cos\theta_2 \end{bmatrix}.$$

The vector $\ddot{r}_{OP}$ represents the absolute translational acceleration in the global inertial system, while $A_{OP}^T \ddot{r}_{OP}$ expresses the same quantity in the body-fixed coordinate system of marker P. The angular acceleration $\dot{\omega}_{OP}$ of marker P is the decomposed expression in its body-fixed coordinate system. Internal force q_{OP} and moment m_{OP} are also expressed in the body-fixed coordinate system at P.

The reduced transformation assumes that half of the state vector can be expressed as a function of the other half. These relationships are referred to as the reduced transfer equations. Consequently, the state vector is divided into two complementary parts, denoted as $z_{a,P}$ and $z_{b,P}$, such that $z_P = \begin{bmatrix} z_b^T & z_a^T \end{bmatrix}_P^T$. It is assumed that $z_{a,P}$ and $z_{b,P}$ are linearly related, expressed as:

$$z_{a,P} = S_P z_{b,P} + e_P, \tag{2}$$

Here, S and e are referred to as the recursive reduced transfer matrices. Importantly, e is external excitation.

Using the kinematic and dynamic equations of body and joint elements, along with the reduced transformation of state vectors at root and tip markers, recursive relationships for the elements are formulated. This approach allows direct computation of S and e at

each marker through recursive relations by passing the need to calculate the transfer matrix for individual elements.

2.3. Reduced Transfer Equation of a Rigid Body

The reduced transfer equations for a rigid body in spatial motion are derived from acceleration-level kinematic and dynamic analyses. Figure 5 depicts a rigid body in spatial motion. The global inertial Cartesian coordinate system, $Oxyz$, is fixed to the ground, while $Rx'y'z'$ represents the body-fixed coordinate system with origin R, the root marker of the rigid body. Point T is an arbitrary tip marker on the rigid body, and C is the center of mass.
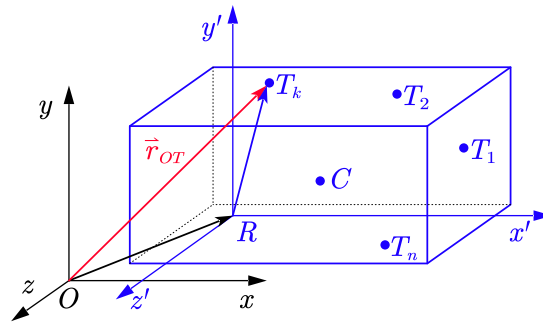
Figure 5. A rigid body in spatial motion. The rigid body is represented as a rectangular prism with feature points, including the center of mass C, root marker R, and tip markers $(T_1, T_2, \cdots, T_k, \cdots, T_n)$. The coordinate systems $Oxyz$ is global inertia system and $Rx'y'z'$ is body-fixed system. Vector r_{OT} represents the position vector from the origin O to tip marker T_k.

A rigid body in spatial motion features a single-root marker R and multiple tip markers $T_1, T_2, \cdots, T_k, \cdots, T_n$. Let point T_k denote the k-th tip marker. The equation for the acceleration vector is projected into the body-fixed coordinate system at this tip marker. The acceleration relationship between the root marker and the k-th tip marker, expressed in the body-fixed coordinate system, is given by the following equations [19,35,36]:

$$A_{OT_k}^{\mathrm{T}} \ddot{r}_{OT_k} = A_{RT_k}^{\mathrm{T}} A_{OR}^{\mathrm{T}} \ddot{r}_{OR} + A_{RT_k}^{\mathrm{T}} \tilde{l}_{RT_k}^{\mathrm{T}} \dot{\omega}_{OR} + A_{RT_k}^{\mathrm{T}} \tilde{\omega}_{OR} \tilde{\omega}_{OR} l_{RT_k} \tag{3}$$

and

$$\dot{\omega}_{OT_k} = A_{RT_k}^{\mathrm{T}} \dot{\omega}_{OR}, \tag{4}$$

where R and T_k represent the root marker and the k-th tip marker of the rigid body, respectively. The vector l_{RT_k} defines the displacement from the root marker R to the k-th tip marker T_k, expressed in the body-fixed coordinate system of R. The notation $\tilde{\bullet}$ denotes the skew-symmetric operator used to compute the cross-product for vector $\bullet$. Skew-symmetric matrices can be used to represent rotational generators in three-dimensional space and are closely related to angular velocity or rigid body motion. In three-dimensional space, skew-symmetric matrices are often used to describe the cross-product operation of a vector. For vector $v = [v_1, v_2, v_3]^{\mathrm{T}}$, you can define a corresponding skew-symmetric matrix $\tilde{v}$:

$$\tilde{v} = \begin{bmatrix} 0 & -v_3 & v_2 \\ v_3 & 0 & -v_1 \\ -v_2 & v_1 & 0 \end{bmatrix}.$$

Equations (3) and (4) can be compactly rewritten as:

$$a_{T_k} = C_{T_k R} a_R + \eta_{T_k}, \tag{5}$$

where

$$a_{T_k} = \begin{bmatrix} A_{OT_k}^T \ddot{r}_{OT_k} \\ \dot{\omega}_{OT_k} \end{bmatrix}, \quad C_{T_k R} = \begin{bmatrix} A_{RT_k}^T & A_{RT_k}^T \tilde{l}_{RT_k}^T \\ O_{3\times3} & A_{RT_k}^T \end{bmatrix},$$

$$a_R = \begin{bmatrix} A_{OR}^T \ddot{r}_{OR} \\ \dot{\omega}_{OR} \end{bmatrix}, \quad \eta_{T_k} = \begin{bmatrix} A_{RT_k}^T \tilde{\omega}_{OR} \tilde{\omega}_{OR} l_{RT_k} \\ O_{3\times1} \end{bmatrix}.$$

Considering the notational conventions of RMSTMM, the dynamic equations projected into the body-fixed coordinate system of the root marker can be expressed as [19]:

$$
\begin{cases}
m A_{OR}^T \ddot{r}_{OR} + m \tilde{l}_{RC}^T \dot{\omega}_{OR} + m \tilde{\omega}_{OR} \tilde{\omega}_{OR} l_{RC} = q_R - \sum_k A_{RT_k} q_{T_k} + q_{R,\mathrm{Ex}}, \\
m \tilde{l}_{RC} A_{OR}^T \ddot{r}_{OR} + \tilde{\omega}_{OR} J_R \omega_{OR} + J_R \dot{\omega}_{OR} = m_R - \sum_k \left(\tilde{l}_{RT_k} A_{RT_k} q_{T_k} + A_{RT_k} m_{T_k} \right) + m_{R,\mathrm{Ex}},
\end{cases}
\tag{6}
$$

where l_{RC} denotes the vector from the root marker R to the center of mass, expressed in the body-fixed coordinate system of R. The inertia tensor of the rigid body, J_R, is expressed in the same body-fixed coordinate system. Symbols $q_{R,\mathrm{Ex}}$ and $m_{R,\mathrm{Ex}}$ denote the resultant external force and moment acting on the root marker R, respectively. Equation (6) can be rewritten in a compact form as:

$$M_R a_R = f_R - \sum_k C_{T_k R}^T f_{T_k} + \beta_R, \tag{7}$$

where

$$M_R = \begin{bmatrix} m I_3 & m \tilde{l}_{RC}^T \\ m \tilde{l}_{RC} & J_R \end{bmatrix}, f_R = \begin{bmatrix} q_R \\ m_R \end{bmatrix}, f_{T_k} = \begin{bmatrix} q_{T_k} \\ m_{T_k} \end{bmatrix}, \beta_R = f_{R,\mathrm{Ex}} - \begin{bmatrix} m \tilde{\omega}_{OR} \tilde{\omega}_{OR} l_{RC} \\ \tilde{\omega}_{OR} J_R \omega_{OR} \end{bmatrix},$$

$f_{R,Ex}$ represents the combined external force acting on the rigid body with respect to its root marker. The reduced transfer equation for the k-th tip marker is assumed to take the following form:

$$f_{T_k} = S_{T_k} a_{T_k} + e_{T_k}, \tag{8}$$

By substituting Equations (5) and (8) into Equation (7), the reduced transfer equation for the root marker can be obtained as follows:

$$f_R = S_R a_R + e_R, \tag{9}$$

where

$$
\begin{cases}
S_R = \sum_k C_{T_k R}^T S_{T_k} C_{T_k R} + M_R, \\
e_R = \sum_k C_{T_k R}^T \left(S_{T_k} \eta_{T_k} + e_{T_k} \right) - \beta_R.
\end{cases}
\tag{10}
$$

Equation (10) shows the recursive relationship for the reduced transfer equation of the rigid body element.

2.4. Reduced Transfer Equation of a Joint

The mass of the joint element is considered negligible. Figure 6 illustrates a joint element in spatial motion, with coordinate system definitions consistent with Figure 5. The root marker and tip marker of the joint element are denoted as R and T, respectively. Depending on the joint type, the tip marker T may move relative to the root marker R.

The acceleration-level kinematic equations for the joint element can be expressed in the coordinate system of the tip marker [19,35,36]:

$$A_{OT}^T \ddot{r}_{OT} = A_{RT}^T A_{OR}^T \ddot{r}_{OR} + A_{RT}^T \tilde{l}_{RT}^T \dot{\omega}_{OR} + A_{RT}^T \ddot{l}_{RT} + A_{RT}^T \left(2 \tilde{\omega}_{OR} \dot{l}_{RT} + \tilde{\omega}_{OR} \tilde{\omega}_{OR} l_{RT} \right) \tag{11}$$

and

$$\dot{\omega}_{OT} = A_{RT}^{\mathrm{T}}\dot{\omega}_{OR} + \dot{\omega}_{RT} + A_{RT}^{\mathrm{T}}\tilde{\omega}_{OR}A_{RT}\omega_{RT}. \tag{12}$$

Combining the two equations

$$\left[\begin{array}{c} A_{OT}^{\mathrm{T}}\ddot{r}_{OT} \\ \dot{\omega}_{OT} \end{array}\right] = \left[\begin{array}{cc} A_{RT}^{\mathrm{T}} & A_{RT}^{\mathrm{T}}\tilde{l}_{RT}^{\mathrm{T}} \\ O_{3\times 3} & A_{RT}^{\mathrm{T}} \end{array}\right]\left[\begin{array}{c} A_{OR}^{\mathrm{T}}\ddot{r}_{OR} \\ \dot{\omega}_{OR} \end{array}\right] + \left[\begin{array}{c} A_{RT}^{\mathrm{T}}\ddot{l}_{RT} \\ \dot{\omega}_{RT} \end{array}\right] + \left[\begin{array}{c} A_{RT}^{\mathrm{T}}\left(2\tilde{\omega}_{OR}\dot{l}_{RT} + \tilde{\omega}_{OR}\tilde{\omega}_{OR}l_{RT}\right) \\ A_{RT}^{\mathrm{T}}\tilde{\omega}_{OR}A_{RT}\omega_{RT} \end{array}\right]. \tag{13}$$

The second term on the right-hand side of the equation represents the relative acceleration of the tip marker T with respect to the root marker R. Assume the relative acceleration term is expressed as:

$$\left[\begin{array}{c} A_{RT}^{\mathrm{T}}\ddot{l}_{RT} \\ \dot{\omega}_{RT} \end{array}\right] = \mathbf{\Phi}\ddot{q} + \xi, \tag{14}$$

where ξ varies depending on the type of joint element. For a revolute joint, $\mathbf{\Phi}$ and ξ are $\begin{bmatrix} 0 & 0 & 0 & 0 & 0 & 1 \end{bmatrix}^{\mathrm{T}}$ and $\mathbf{0}_{6\times 1}$, respectively. For a translational joint, $\mathbf{\Phi}$ and ξ are $\begin{bmatrix} 0 & 0 & 1 & 0 & 0 & 0 \end{bmatrix}^{\mathrm{T}}$ and $\mathbf{0}_{6\times 1}$, respectively.

Subsequently, Equation (13) can be compactly rewritten as

$$a_T = C_{TR}a_R + \mathbf{\Phi}\ddot{q} + \eta, \tag{15}$$

where

$$a_T = \left[\begin{array}{c} A_{OT}^{\mathrm{T}}\ddot{r}_{OT} \\ \dot{\omega}_{OT} \end{array}\right], C_{TR} = \left[\begin{array}{cc} A_{RT}^{\mathrm{T}} & A_{RT}^{\mathrm{T}}\tilde{l}_{RT}^{\mathrm{T}} \\ O_{3\times 3} & A_{RT}^{\mathrm{T}} \end{array}\right],$$

$$a_R = \left[\begin{array}{c} A_{OR}^{\mathrm{T}}\ddot{r}_{OR} \\ \dot{\omega}_{OR} \end{array}\right], \eta = \xi + \left[\begin{array}{c} A_{RT}^{\mathrm{T}}\left(2\tilde{\omega}_{OR}\dot{l}_{RT} + \tilde{\omega}_{OR}\tilde{\omega}_{OR}l_{RT}\right) \\ A_{RT}^{\mathrm{T}}\tilde{\omega}_{OR}A_{RT}\omega_{RT} \end{array}\right].$$

A force analysis of the joint element is performed to determine the internal force relationship between the root and tip markers. The internal force at the tip marker is decomposed into applied forces and constraint forces, expressed as [37]:

$$f_T = \mathbf{\Psi}\lambda + \mathbf{\Psi}_C\lambda_C, \tag{16}$$

where f_T represents the internal force and torque at the tip marker. $\mathbf{\Psi}\lambda$ denotes the applied force, while $\mathbf{\Psi}_C\lambda_C$ represents the constraint force.

Figure 6. A joint element in spatial motion. Joints have only one root marker R and one tip marker T, no matter what type.

Assume that the reduced transfer equation for the tip marker of the joint element is given by:

$$f_T = S_T a_T + e_T. \tag{17}$$

The generalized acceleration can be derived by combining Equations (15)–(17), resulting in:

$$\ddot{\boldsymbol{q}} = \boldsymbol{Q}_a \boldsymbol{a}_R + \boldsymbol{Q}_0, \tag{18}$$

where

$$\begin{cases} \boldsymbol{Q}_a = -\boldsymbol{M}^{-1}\boldsymbol{\Phi}^{\mathrm{T}}\boldsymbol{S}_T\boldsymbol{C}_{TR} \\ \boldsymbol{Q}_0 = \boldsymbol{M}^{-1}[\boldsymbol{\lambda} - \boldsymbol{\Phi}^{\mathrm{T}}(\boldsymbol{S}_T\boldsymbol{\eta} + \boldsymbol{e}_T)] \end{cases}, \quad \boldsymbol{M} = \boldsymbol{\Phi}^{\mathrm{T}}\boldsymbol{S}_T\boldsymbol{\Phi}. \tag{19}$$

The internal force relationship for the intermediate connection marker is derived and utilized to analyze the internal forces at the root and tip markers. It is expressed as:

$$\boldsymbol{f}_R = \boldsymbol{C}_{TR}^{\mathrm{T}}\boldsymbol{f}_T, \tag{20}$$

where $\boldsymbol{f}_R$ represents the internal force and moment at the root marker. By substituting Equation (18) into Equation (15), the acceleration relationship between the root marker and the tip marker is obtained:

$$\boldsymbol{a}_T = \boldsymbol{A}_a \boldsymbol{a}_R + \boldsymbol{A}_0, \tag{21}$$

where

$$\begin{cases} \boldsymbol{A}_a = \boldsymbol{C}_{TR} + \boldsymbol{\Phi}\boldsymbol{Q}_a \\ \boldsymbol{A}_0 = \boldsymbol{\Phi}\boldsymbol{Q}_0 + \boldsymbol{\eta} \end{cases}. \tag{22}$$

The reduced transfer equation for the tip marker of the joint element is derived by combining Equations (17), (20), and (21) and is expressed as:

$$\boldsymbol{f}_R = \boldsymbol{S}_R \boldsymbol{a}_R + \boldsymbol{e}_R, \tag{23}$$

where

$$\begin{cases} \boldsymbol{S}_R = \boldsymbol{C}_{TR}^{\mathrm{T}}\boldsymbol{S}_T\boldsymbol{A}_a \\ \boldsymbol{e}_R = \boldsymbol{C}_{TR}^{\mathrm{T}}(\boldsymbol{S}_T\boldsymbol{A}_0 + \boldsymbol{e}_T) \end{cases}. \tag{24}$$

Equation (24) represents the recursive relationship for the reduced transfer equation of the joint element.

2.5. Solution Procedures of the Vehicle System Dynamics

The overall procedure for solving the vehicle system dynamics using RMSTMM is shown in Figure 7 and can be summarized as follows:

Step 1 Using the initial configuration of the multibody system, the initial conditions, including generalized coordinates and velocities, are determined.

Step 2 By performing a kinematic analysis from the root marker to the tip markers, the positions and velocities of the intermediate connection markers at the current time step are calculated based on the generalized coordinates and velocities.

Step 3 The reduced transfer equations for the tip markers are established using their boundary conditions. These equations are then recursed backward, from the tip markers to the root marker, to compute the reduced transfer equations for the entire system.

Step 4 Using the boundary conditions at the root marker, the state vector of the root marker is determined. This information is then recursed forward, from the root marker to the tip markers, to calculate the state vector and the generalized accelerations for the entire system.

Step 5 Numerical methods such as the Runge–Kutta method are applied to update the generalized coordinates and velocities for the next time step.

Step 6 The process returns to Step 2, and the updated generalized coordinates and velocities are adopted to repeat until the required analysis time is reached.
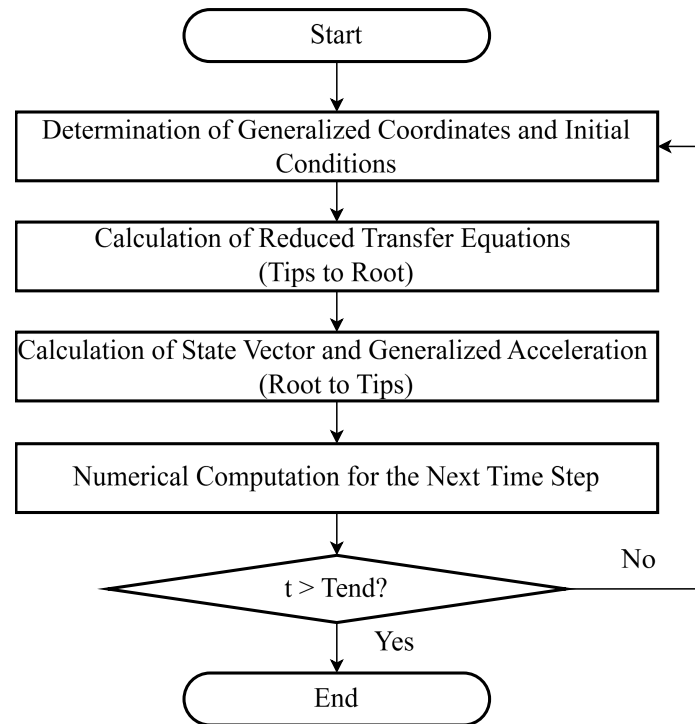
Figure 7. Vehicle system dynamics solution process using RMSTMM.

3. Modeling of External Forces and Road Surface

3.1. Contact Model

The wheel is modeled as a rigid body, with the contact force between the wheel and the ground described using Hertz's classical contact theory [38].

The dashed line in the figure represents the reference road surface position. The radius of the wheel is denoted by R. The contact depth is defined as δ. For a level road surface, as illustrated in Figure 8a, no contact force occurs if $\delta \geqslant 0$. Conversely, when $\delta < 0$, a contact force is generated. For an uneven road surface, as depicted in Figure 8b, the displacement of the road surface at the contact point relative to the reference position is denoted as r, where the positive r direction aligns with the y axis. A contact force does not occur if $\delta - r \geqslant 0$. If $\delta - r < 0$, a contact force is generated, with the contact depth defined as $r - \delta$.
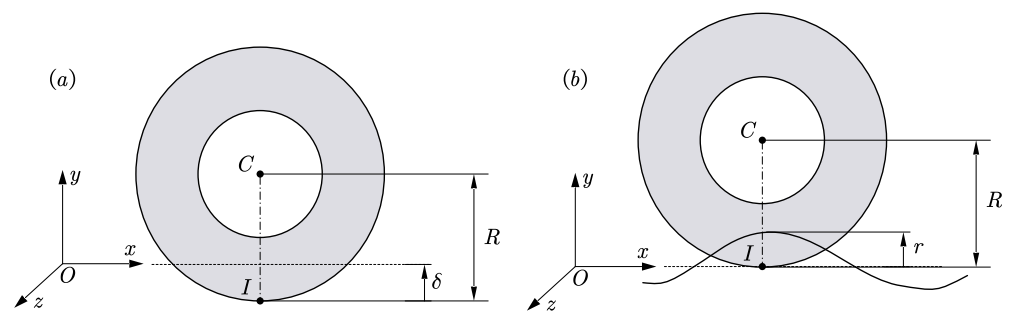
Figure 8. Wheel and ground contact model. The center of mass of the wheel is denoted as C, and the radius is denoted as R. (**a**) Represents a level road surface where the contact depth δ is minimal. (**b**) Depicts an uneven road surface with the contact depth r varying to accommodate surface irregularities.

The magnitude of the contact force primarily depends on the stiffness, damping, and contact depth of the interacting objects. This force generally comprises two components: an elastic force, resembling a nonlinear spring, and a damping force, dependent on

the deformation velocity. The mathematical representation of the contact force model is given by:

$$F = \begin{cases} -K(\delta - r)^{\alpha} - C_{\max}\dot{\delta} \cdot step(r - \delta, d, 1, 0, 0) & , \quad y \leqslant r, \\ 0 & , \quad \delta > r, \end{cases} \tag{25}$$

where δ is considered to be generalized displacement, $\dot{\delta}$ is the generalized velocity, K denotes the contact stiffness, a is the nonlinear exponent of the contact force, C_{max} is the maximum damping coefficient during contact, d is the maximum contact depth, and *step* is a step function used to prevent discontinuities in the damping component when the contact force changes abruptly. Specifically, the damping component is zero when the contact depth is zero and reaches C_{max} at the maximum contact depth. The *step* function is expressed as:

$$step(\tau, d, h_0, 0, h_1) = \begin{cases} h_1 & , \quad \tau \leqslant 0, \\ h_0 = (h_1 - h_0)\Delta^2(3 - 2\Delta) & , \quad 0 < \tau < d, \\ h_0 & , \quad \tau \geqslant d, \end{cases} \tag{26}$$

where $\tau = r - \delta$ represents the contact depth. $\Delta = (d - \tau)/d, h_0 = 1, h_1 = 0$.

3.2. Friction Model

During vehicle motion, frictional force acts between the wheel and the ground. The friction force model in this paper is based on the following assumptions: (1) The frictional force is independent of the contact area. (2) Its direction opposes the relative velocity between the two objects. (3) Its magnitude is proportional to the normal contact pressure. The tangential frictional force, F_x, is analyzed under three scenarios:

1. No Contact: The normal contact force F_y is zero.

$$F_x = 0. \tag{27}$$

2. Pure Rolling: The velocity at the contact point between the wheel and the ground is zero. According to Coulomb's law, the magnitude of the frictional force is described by the equation:

$$|F_x| \leqslant \mu_0 F_y, \tag{28}$$

where μ_0 is the coefficient of static friction. The corresponding moment balance leads to the equation:

$$F_x = -\frac{M_c}{R}. \tag{29}$$

3. Rolling and Sliding: When the wheel undergoes both rolling and sliding, Coulomb's law governs the frictional force, expressed by the equation:

$$F_x = -\mu F_y \cdot \text{sgn}(M_c), \tag{30}$$

where μ is the coefficient of kinetic sliding friction.

Consequently, the tangential frictional force is expressed as:

$$F_x = \begin{cases} 0 & , \quad F_{y=0}, \\ -M_c/R & , \quad |M_c|/R \leqslant \mu_0 F_y, \\ -\mu F_y \text{sgn}(M_c) & , \quad |M_c|/R > \mu_0 F_y. \end{cases} \tag{31}$$

3.3. Road Surface

Figure 9 demonstrates the application of the harmonic superposition method [39] to generate an unevenness profile corresponding to Class C, D, and E road surface conditions. The unevenness magnitude of Class D road mostly ranges from ±0.10 m, not more than ±0.15 m and a total road length of 2000 m is analyzed. The simulated road file results accurately capture the stochastic features and high-frequency disturbances characteristic of Class D road surfaces. Based on this input, the effects of suspension and tire models on the dynamic behavior of vehicles are assessed using RMSTMM dynamics equations.
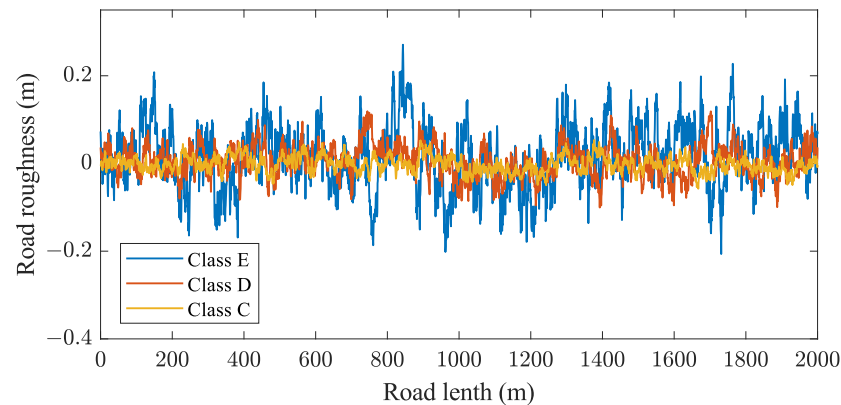
Figure 9. Road roughness profiles for Class C, D, and E road surfaces over a 2000 m stretch. The varying amplitudes highlight the increasing severity of unevenness from Class C to Class E.

4. Numerical Results

4.1. Simulation Model and Conditions

To study the dynamic response characteristics of the vehicle under complex road conditions, this study utilizes the dynamic equations of the vehicle model, in conjunction with the simulation model parameters presented in Table 2, to perform numerical calculations. The specific vehicle parameters include key geometric and mass characteristics, including body dimensions, wheelbase, and mass distribution. The vehicle is rear-wheel drive.

Table 2. Dimensions and weights of the vehicle.

Parameter	Value
Length	4143 mm
Width	1817 mm
Height	1300 mm
Wheelbase	2430 mm
Front track	1550 mm
Rear track	1567 mm
Distance of CG from front axle	1214.5 mm
Distance of CG from rear axle	1215.5 mm
Front-Wheel Radius	318.6 mm
Rear-Wheel Radius	314.35 mm
Curb weight	1580 Kg
Damper weight	8 Kg
Wheel weight	30 Kg
Suspension spring stiffness	30,000 N/m
Suspension damping coefficient	3000 N·s/m
Tire stiffness	290,000 N/m
Tire damping coefficient	3100 N·s/m

4.2. Simulation Results

The dynamic performance of the vehicle was simulated and analyzed using the RMSTMM and a complete vehicle model under Class D road surface unevenness at a speed of 40 km/h. The accuracy of the RMSTMM approach is validated with ADAMS simulation, as is shown in Figure 10. The time response results for the vertical acceleration of the vehicle body center of mass, the dynamic deflection of the front suspension system, and the angular acceleration of the vehicle body center of mass are presented in Figures 11–13, respectively.
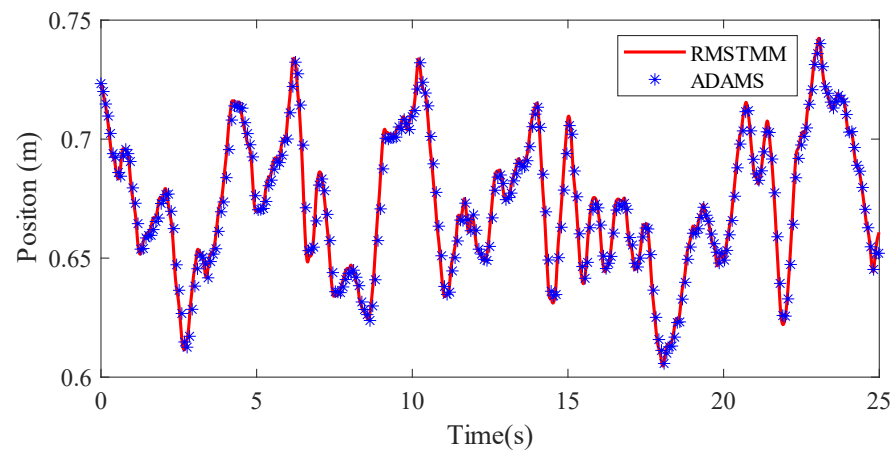
Figure 10. Comparison of the vertical position response of the vehicle body center of mass as obtained from RMSTMM and ADAMS simulations at a speed of 40 km/h under Class D road surface. The close agreement between the two methods validates the accuracy of the RMSTMM approach.
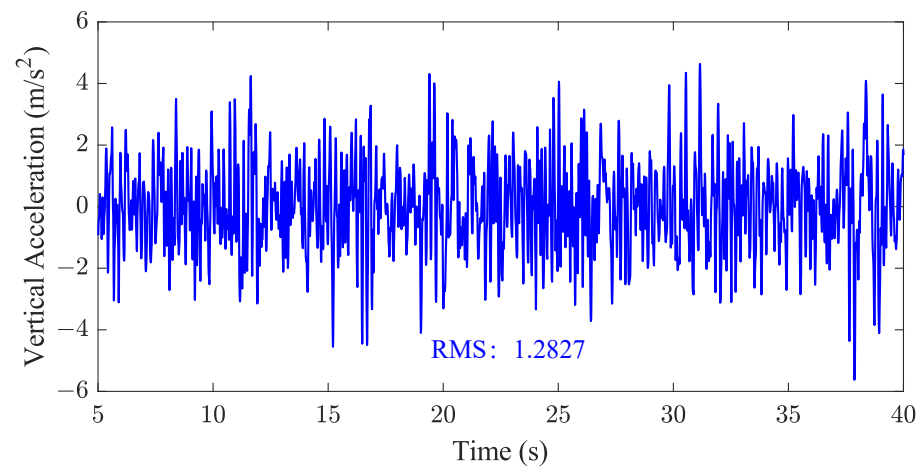
Figure 11. Vertical acceleration response of the vehicle body center of mass over time. The plot shows the dynamic effects of road irregularities on the vehicle, with an RMS value of 1.2827 m/s^2.

Figure 11 shows the vertical acceleration response of the vehicle body center of mass. The simulation results reveal that the peak vertical acceleration under Class D road conditions is within ±6 m/s^2, demonstrating the significant effect of road input excitation on ride comfort. High-frequency fluctuations in acceleration may cause driver discomfort, emphasizing the need to improve the vibration isolation performance of the suspension system.

Figure 12 depicts the dynamic deflection response of the front suspension system, with maximum deflections ranging from 0.08 m to 0.18 m. These fluctuations reflect the dynamic behavior of suspension systems under complex road inputs. Larger deflections may lead to suspension under-travel or overload issues, underscoring the importance of optimally matching spring stiffness and damping coefficients.

Figure 13 illustrates the angular acceleration response of the vehicle body center of mass. The peak angular acceleration, approximately ±5 rad/s^2, indicates significant pitching and swaying dynamics under Class D road conditions. Such dynamics may negatively impact the ride stability and handling performance.
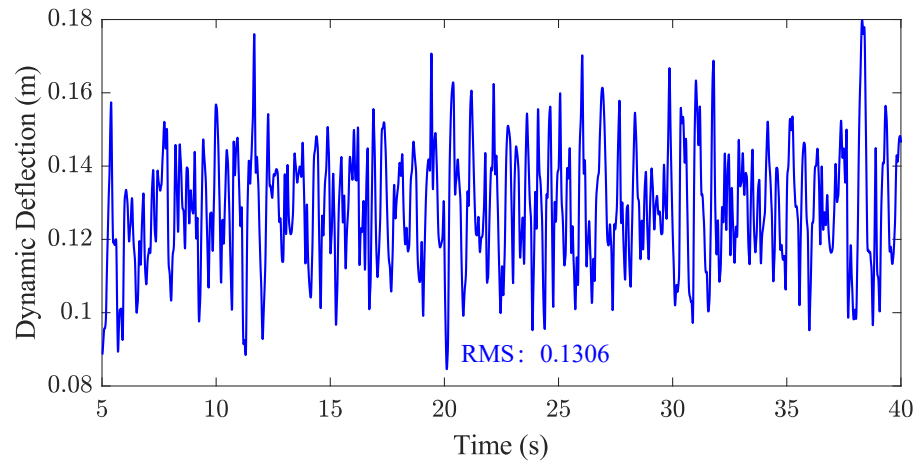
Figure 12. Dynamic deflection response of the front suspension system over time. The plot highlights the suspension travel due to road-induced loads, with an RMS value of 0.1306 m.
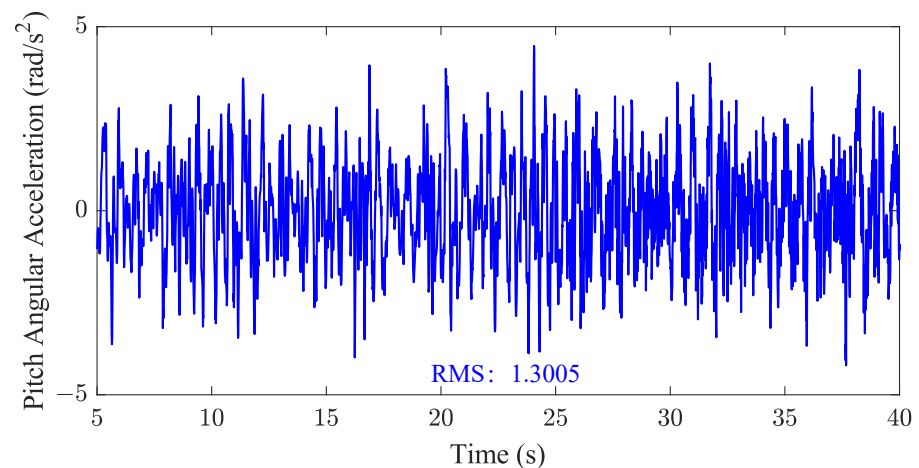
Figure 13. Pitch angular acceleration response of the vehicle body center of mass over time. The plot illustrates the rotational dynamics caused by road unevenness, with an RMS value of 1.3005 rad/s^2.

Overall, the simulation results demonstrate the limitations of the current suspension system in isolating high-frequency vibrations under Class D road conditions. Significant fluctuations in vertical and angular accelerations at the body center of mass highlight the necessity for optimizing suspension parameters to improve vehicle comfort and stability.

5. Suspension Parameters Optimization

Based on the results of the simulation analysis of the initial parameters, significant potential remains for improving the current vehicle performance, particularly regarding the vertical acceleration of the body center-of-mass and suspension deflection. In this section, an optimization algorithm is employed to iteratively refine the design variables and evaluate their impact on vehicle dynamics.

5.1. Objective Function

The vertical acceleration of the car body centroid is an important index of vehicle riding comfort. Higher vertical acceleration can cause the occupants of the vehicle to

experience severe vibration, which reduces comfort. Optimizing this index can directly reduce the vertical vibration of the vehicle on uneven road surfaces and reduce the adverse effects of vibration on the human body.

The dynamic deflection of suspension reflects the working range of the suspension system and is an important parameter to measure the effectiveness of the suspension system. Excessive dynamic deflection may lead to insufficient travel or overload of the suspension system, affecting the handling and durability of the vehicle. Optimizing the dynamic deflection of the suspension helps to better absorb the shock on the uneven road surface while avoiding the failure of the suspension system due to excessive deformation.

The pitch angle acceleration of the car body center of mass represents the longitudinal pitch motion of the vehicle, which directly affects the driving stability and safety of the vehicle. Excessive pitch movement will affect the driver's control of the vehicle and increase the difficulty of operation. Optimizing this index can effectively reduce the pitch motion caused by uneven road surfaces, improve the dynamic stability of the vehicle, help prevent the drastic change in load between the front and rear wheels of the vehicle, and improve the contact between the tire and the ground.

These three objectives comprehensively consider vehicle performance from three key perspectives: ride comfort, suspension effectiveness, and vehicle dynamic stability. There is a certain coupling relationship between these three objectives. It is necessary to weigh and balance the optimization process to ensure the comprehensive improvement of each performance index. Based on complex road conditions and different speeds, optimizing these targets can better meet user needs and enhance vehicle competitiveness. For this reason, the optimization objective function is defined as:

$$
\min \boldsymbol{F}(\boldsymbol{x}) = \begin{bmatrix} F_1(\boldsymbol{x}) & F_2(\boldsymbol{x}) & F_3(\boldsymbol{x}) \end{bmatrix}^{\mathrm{T}}, \tag{32}
$$

where

$$
F_1(\boldsymbol{x}) = \mathrm{RMS}(\ddot{y}_c), F_2(\boldsymbol{x}) = \mathrm{RMS}(\delta_d), F_3(\boldsymbol{x}) = \mathrm{RMS}(\dot{\omega}_c).
$$

$\mathrm{RMS}(\ddot{y}_c)$ represents the RMS value of the vertical acceleration at the center of mass of the vehicle body, characterizing the smoothness performance of the vehicle. $\mathrm{RMS}(\delta_d)$ is the RMS value of suspension deflection used to evaluate the dynamic response characteristics of the suspension system. $\mathrm{RMS}(\dot{\omega}_c)$ denotes the RMS value of the center-of-mass angular acceleration of the vehicle body, reflecting the dynamic stability.

The three objectives are interdependent, and adjusting one objective can negatively impact the others. For example, reducing the RMS of suspension deflection could increase the vertical acceleration of the vehicle body. Therefore, the optimization process usually employs a multi-objective optimization strategy to achieve an optimal trade-off, resulting in a set of solutions that balance all objectives.

5.2. Design Variables

To enhance smoothness and dynamic performance under complex road conditions, the suspension stiffness k_2, k_6, k_{10} and k_{14} and damping parameters c_2, c_6, c_{10} and c_{14} are selected as the design variables. k_2, k_6, c_2, c_6 are the stiffnesses and damping coefficients of the front suspension. k_{10}, k_{14}, c_{10} and c_{14} are the stiffnesses and damping coefficients of the rear suspension. It is generally assumed that the two front suspension parameters are identical, and the two rear suspension parameters are identical. Therefore, this paper recognizes $k_2 = k_6 = K_f$, $c_2 = c_6 = C_f$, $k_{10} = k_{14} = K_r$, $c_{10} = c_{14} = C_r$. The design variables are defined as follows:

$$
\boldsymbol{x} = \begin{bmatrix} K_f & C_f & K_r & C_r \end{bmatrix}^{\mathrm{T}}, \tag{33}
$$

where K_f and K_r are the stiffnesses of the front and rear suspensions, respectively, and C_f and C_r are the damping coefficients of the front and rear suspensions, respectively. Their initial values and constraint ranges are shown in Table 3:

Table 3. Initial values and constraint ranges of design variables.

Design Variables	Initial Value	Lower Bound	Upper Bound
K_f, K_r	30,000 N/m	20,000 N/m	50,000 N/m
C_f, C_r	3000 N·m/s	2000 N·m/s	5000 N·m/s

5.3. Optimization Algorithm

To achieve multi-objective optimization of the suspension parameters, this paper utilizes the NSGA-II for optimization. The NSGA-II algorithm is a widely used approach in multi-objective optimization, known for its efficient nondominated sorting strategy and elite retention mechanism. The key features of the algorithm consist of fast, nondominated sorting, elite strategy, and distance-based selection. Fast, nondominated sorting ranks populations based on dominance, effectively distinguishing between solutions. The elite strategy combines and sorts parent and child populations to ensure superior solutions are retained for the next generation. The algorithm also calculates crowding distance to evaluate solution distribution, prioritizing uniformly distributed solutions to enhance diversity. The specific process of NSGA-II (see Figure 14) is as follows, and relevant parameters are summarized in Table 4:

Step 1 Population Merge: merge the current population P_t and the descendant population Q_t into R_t;

Step 2 Nondominated Sorting: perform a fast nondominated sort on R_t to generate multiple nondominated solution fronts $F_0, F_1, \ldots$;

Step 3 Initialize new population: set the next-generation population P_{t+1} to be the empty set with sorting frontier index $i = 1$;

Step 4 Population filling: add individuals in the nondominated solution frontier F_i to P_{t+1} sequentially until the population size reaches the upper limit N;

Step 5 Crowding distance sorting: when a frontier F_i exceeds the upper limit of the population, sort them according to the crowding distance and prioritize the individuals with wider distribution;

Step 6 Generate child population: generate new population Q_{t+1} by crossover, mutation, and other operations;

Step 7 Iterative update: update the number of generations $t = t + 1$ and repeat the above steps until the termination condition is satisfied.

Table 4. NSGA-II algorithm parameters.

Parameters	Value
Population size	100
Number of generations	100
Crossover rate	0.9
Mutation rate	0.033
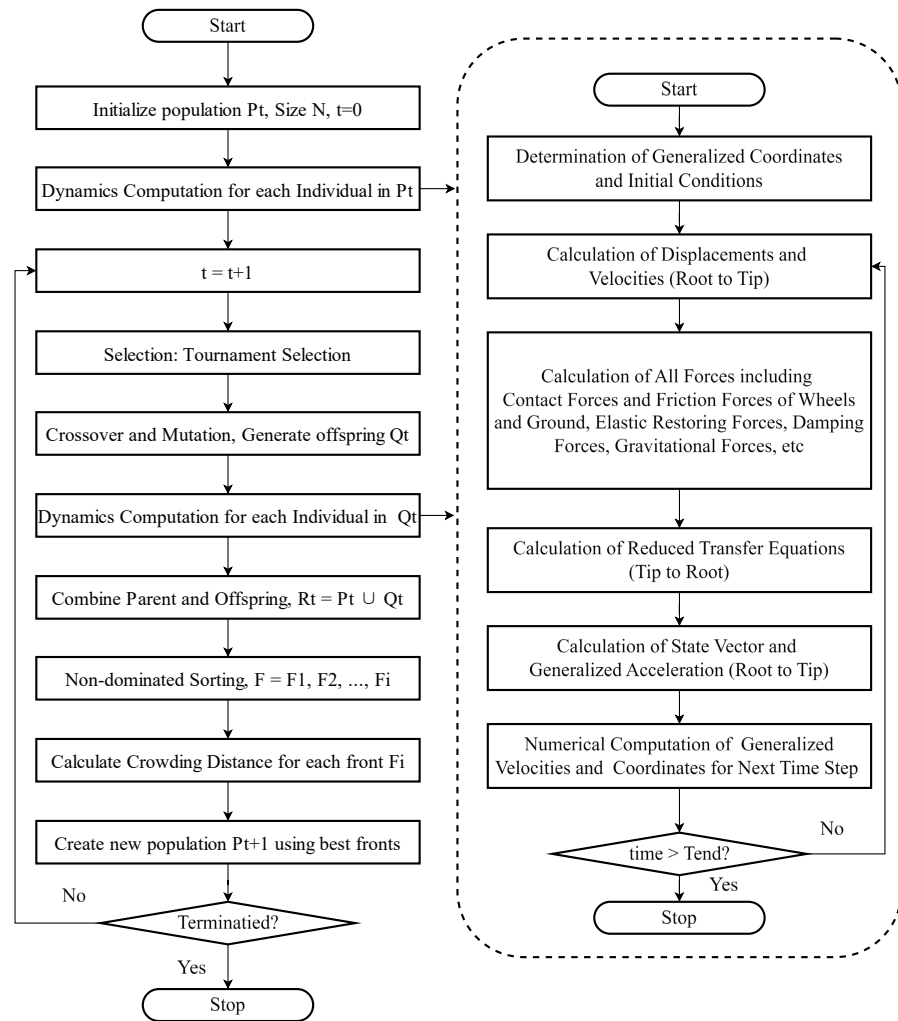
Figure 14. Overall flowchart of the entire optimization process, integrated NSGA-II with RMSTMM.

5.4. Results Analysis

The multi-objective optimization of the suspension stiffness and damping parameters using the NSGA-II algorithm was conducted, and the resulting Pareto frontier distribution is depicted in Figure 14. The optimization objectives include the RMS values of the body center-of-mass vertical acceleration, suspension dynamic deflection, and body center-of-mass angular acceleration.

The optimization results reveal a degree of conflict between suspension dynamic deflection and body angular acceleration when attempting to reduce body vertical acceleration. This trade-off relationship is a common phenomenon in multi-objective optimization of suspension systems, highlighting that simultaneous optimization of all objectives is unattainable through simple adjustments.

The trade-off relationship between the objectives is detailed as follows:

- RMS($\ddot{y}_c$) vs. RMS(δ_d) (Figure 15b)

  The results demonstrate a clear trade-off, where reducing the RMS of suspension dynamic deflection RMS(δ_d) leads to an increase in vehicle body sag acceleration RMS($\ddot{y}_c$). This indicates that improved suspension deflection control may compromise ride comfort.

- RMS($\ddot{y}_c$) vs. RMS($\dot{\omega}_c$) (Figure 15c)

  The results reveal that as suspension deflection RMS($\ddot{y}_c$) decreases, the vehicle angular acceleration RMS($\dot{\omega}_c$) generally increases. However, this relationship exhibits

significant scatter, indicating the potential for some configurations to improve both objectives simultaneously.

- RMS(δ_d) vs. RMS($\dot{\omega}_c$) (Figure 15d)

  The optimization results highlight a coupling between suspension dynamic deflection RMS(δ_d) and angular acceleration RMS($\dot{\omega}_c$). Some parameter adjustments can effectively reduce both, but aggressive optimization of one may lead to significant trade-offs in the other.
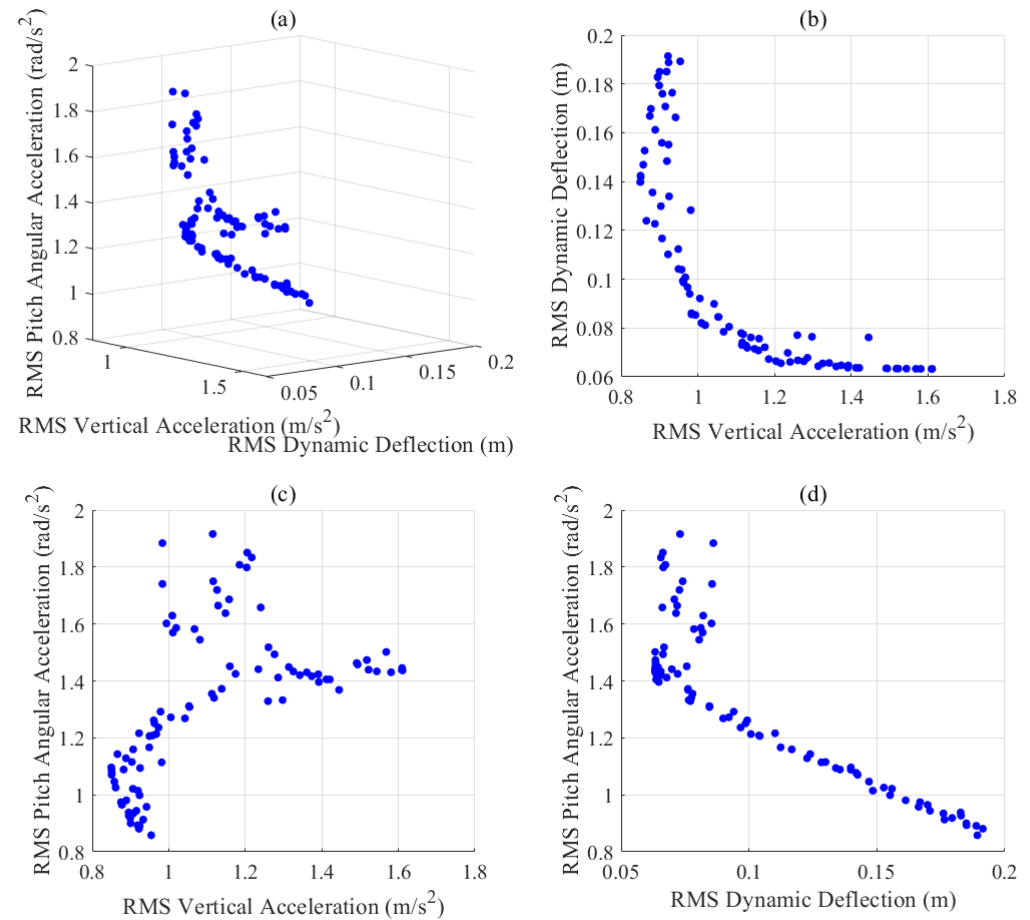
Figure 15. Pareto solution set after 100 iterations of the optimization process, visualizing the trade-offs between different performance metrics. (**a**) 3D Pareto front illustrating the relationships among RMS vertical acceleration, RMS dynamic deflection, and RMS pitch angular acceleration. (**b**) Trade-off curve between RMS vertical acceleration and RMS dynamic deflection, showing an inverse relationship. (**c**) Trade-off curve between RMS vertical acceleration and RMS pitch angular acceleration, highlighting the competing objectives of ride comfort and stability. (**d**) Relationship between RMS dynamic deflection and RMS pitch angular acceleration, illustrating the impact of suspension performance on vehicle stability.

The Pareto front of optimization solutions offers a range of trade-off options for suspension design. For prioritizing ride comfort, solutions with lower RMS($\ddot{y}_c$) are ideal, while enhancing dynamic stability requires selecting solutions with reduced RMS($\dot{\omega}_c$). To achieve a balance between suspension travel utilization and vehicle stability, a compromise can be made between RMS(δ_d) and RMS($\dot{\omega}_c$). These choices enable tailored performance optimization based on specific design priorities.

Based on the set of Pareto solutions, a Pareto frontier can be constructed in the objective space, as shown in Figure 15. The Pareto frontier provides a set of nondominated solutions to a multi-objective optimization problem, demonstrating the trade-offs between

the optimization objectives. However, in order to select a representative optimization solution from the set of solutions, a characteristic point close to the optimal value of all objectives needs to be further determined. To identify a representative solution from this set, a characteristic point approximating the optimal balance among objectives needs to be selected for practical implementation.

Considering that ride comfort, suspension system effectiveness, and vehicle dynamic stability are all important vehicle performance indicators, it is assumed that these three indicators are equal in weight. Therefore, the objective normalized minimum distance method is used to select the optimized value of parameters, which is formulated as:

$$\min d = \sqrt{\sum_{i=1}^{n} \left(\frac{P_i - P_{i,\min}}{P_{i,\max} - P_{i,\min}} \right)^2},$$

(34)

where d is the minimum distance from the Pareto frontier to the Utopia point, P_i is the i-th objective value, and $P_{i,\min}$ and $P_{i,\max}$ are the minimum and maximum values of this objective, respectively. By calculation, the solution corresponding to the minimum distance is the optimized point of the optimization problem. The parameter pairs of optimization initial value and optimized value are shown in Table 5:

Table 5. Comparison of optimized value with initial value.

	K_f (N/m)	C_f (N·m/s)	K_r (N/m)	C_r (N·m/s)	RMS($\ddot{y}_c$) (m/s^2)	RMS(δ_d) (m)	RMS($\dot{\omega}_c$) (rad/s^2)
Initial	30,000	3000	30,000	3000	1.2827	0.1306	1.3005
Optimized	39,757.5	1631.01	20,581.7	1370.78	0.9733	0.0967	1.2364
Ratio	—	—	—	—	−24.12%	−25.98%	−4.931%

These adjustments highlight a strategic shift towards enhancing the dynamic response capability of the suspension system, with the front suspension playing a more critical role in balancing overall vehicle performance. The optimization results demonstrate a significant improvement in the dynamic response of vehicles under Class D road and 40 km/h conditions, as demonstrated by the reduced fluctuation ranges in the key performance metrics.

The vertical acceleration of the vehicle body center of mass, initially ranging from −5.62 to 4.63 m/s^2, was reduced to 3.53 to 3.32 m/s^2 after optimization, reflecting enhanced ride comfort through the mitigation of extreme vertical oscillations. Additionally, the optimized vertical acceleration RMS($\ddot{y}_c$) was reduced by 24.12%, significantly improving ride smoothness (Figure 16).

The suspension dynamic deflection, which originally fluctuated between 0.08 and 0.18 m, decreased to a range of 0.04 to 0.16 m. This indicates a more controlled and stable suspension response, minimizing the risks of under-travel or overload. The suspension dynamic deflection RMS(δ_d) was reduced by 25.98%, effectively controlling suspension travel fluctuations (Figure 17).

The angular acceleration of the vehicle's center of mass, initially spanning −4.20 to 4.48 rad/s^2, was constrained to a narrower range of −4.05 to 3.95 rad/s^2. This reduction signifies improved vehicle stability with minimized pitching and swaying motions. The angular acceleration RMS($\dot{\omega}_c$) was reduced by 4.93%, reflecting enhanced dynamic stability (Figure 18).
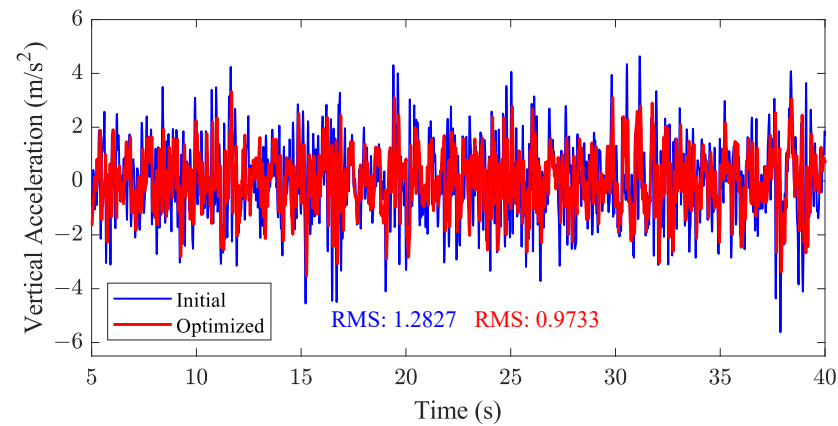
Figure 16. Comparison of vertical acceleration response of the vehicle body center of mass between the initial configuration and the optimized configuration. The RMS value is reduced from 1.2827 m/s² (Initial) to 0.9733 m/s² (Optimized), highlighting a significant improvement in ride comfort.
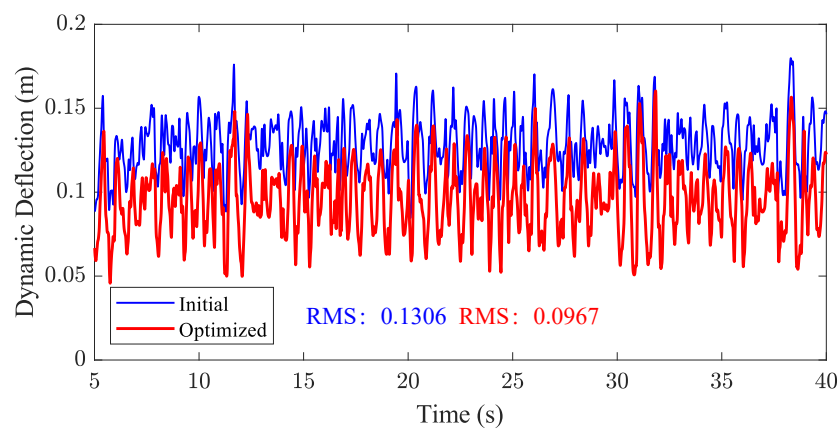
Figure 17. Comparison of dynamic deflection response of the front suspension system between the initial configuration and the optimized configuration. The RMS value decreases from 0.1306 m (Initial) to 0.0967 m (Optimized), demonstrating enhanced suspension performance with reduced suspension travel.
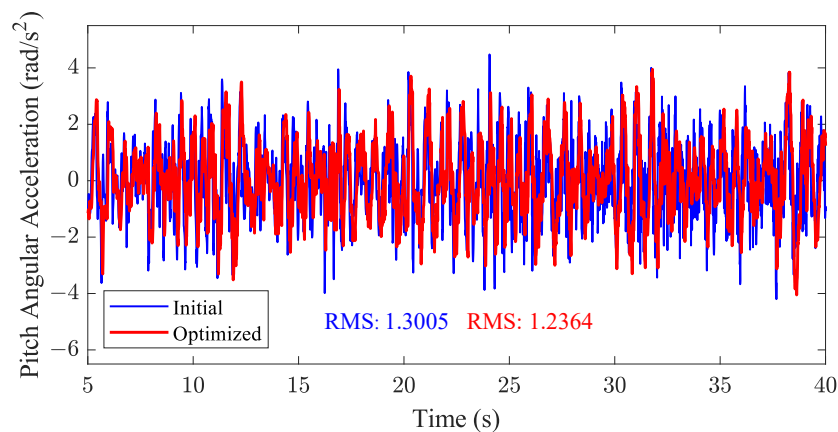
Figure 18. Comparison of angular acceleration response of the vehicle body center of mass between the initial configuration and the optimized configuration. The RMS value reduces from 1.3005 rad/s² (Initial) to 1.2364 rad/s² (Optimized), indicating improved vehicle stability by mitigating pitch motion.

The optimized results indicate that through the adjustment of suspension parameters, the overall vehicle dynamics performance can be significantly improved. The robustness of the optimization results is verified, and the dynamic simulation of Class C, D, and E road conditions is completed at 30 km/h, 40 km/h, and 50 km/h. The frequency response of

the vertical acceleration of the vehicle's centroid before and after optimization is shown in Figure 19. The optimization significantly reduces the vibration amplitude, especially in the low-frequency range (0–5 Hz) and mid-frequency range (5–10 Hz). In the high-frequency range (10–15 Hz), the difference between the initial and optimization results is small, but there is still some improvement.
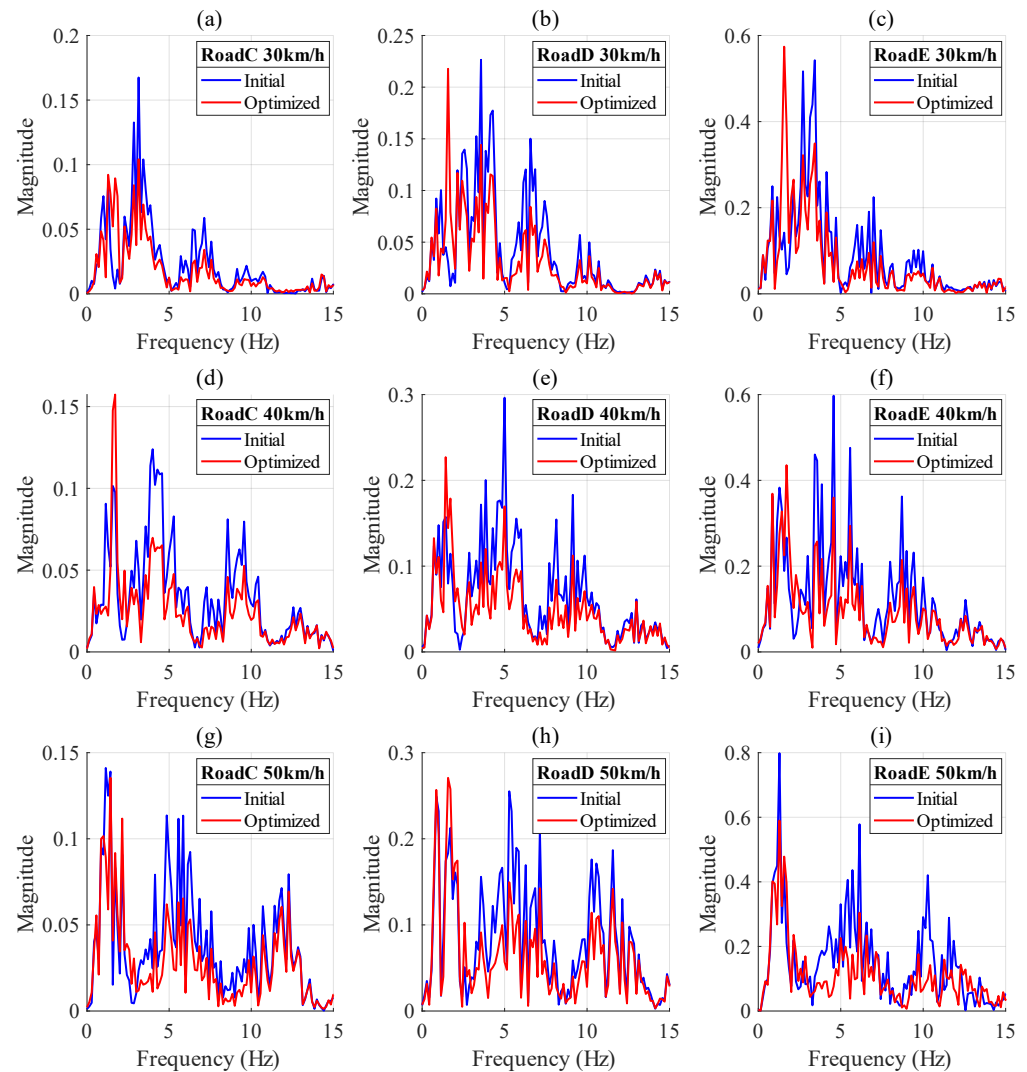
Figure 19. Comparison of the frequency response of vertical acceleration for the vehicle body center of mass across different road types and speeds. The optimized configuration (red) shows reduced magnitude across low- and mid-frequency ranges (0–10 Hz), indicating improved ride comfort and effective suspension dynamics under varying conditions.

The PSD analysis of the vertical acceleration of the vehicle centroid is carried out, and the PSD curves before and after optimization are compared, as is shown in Figure 20. The results show that in all cases, the optimized PSD curves are lower than the initial curves, especially in the range of 4–8 Hz, which is considered to be the most critical frequency range for passenger comfort.

The RMS analysis of vertical acceleration of vehicle centroid is carried out in Figure 21. The optimized value is lower than the initial value at all road types and speeds. Class E road exhibits the highest RMS vertical acceleration, reflecting the challenging nature of its rough pavement. The RMS value increases with speed, but so does the absolute improvement in optimization, especially on rough surfaces and at high speeds, where the maximum improvement is 27.32%.
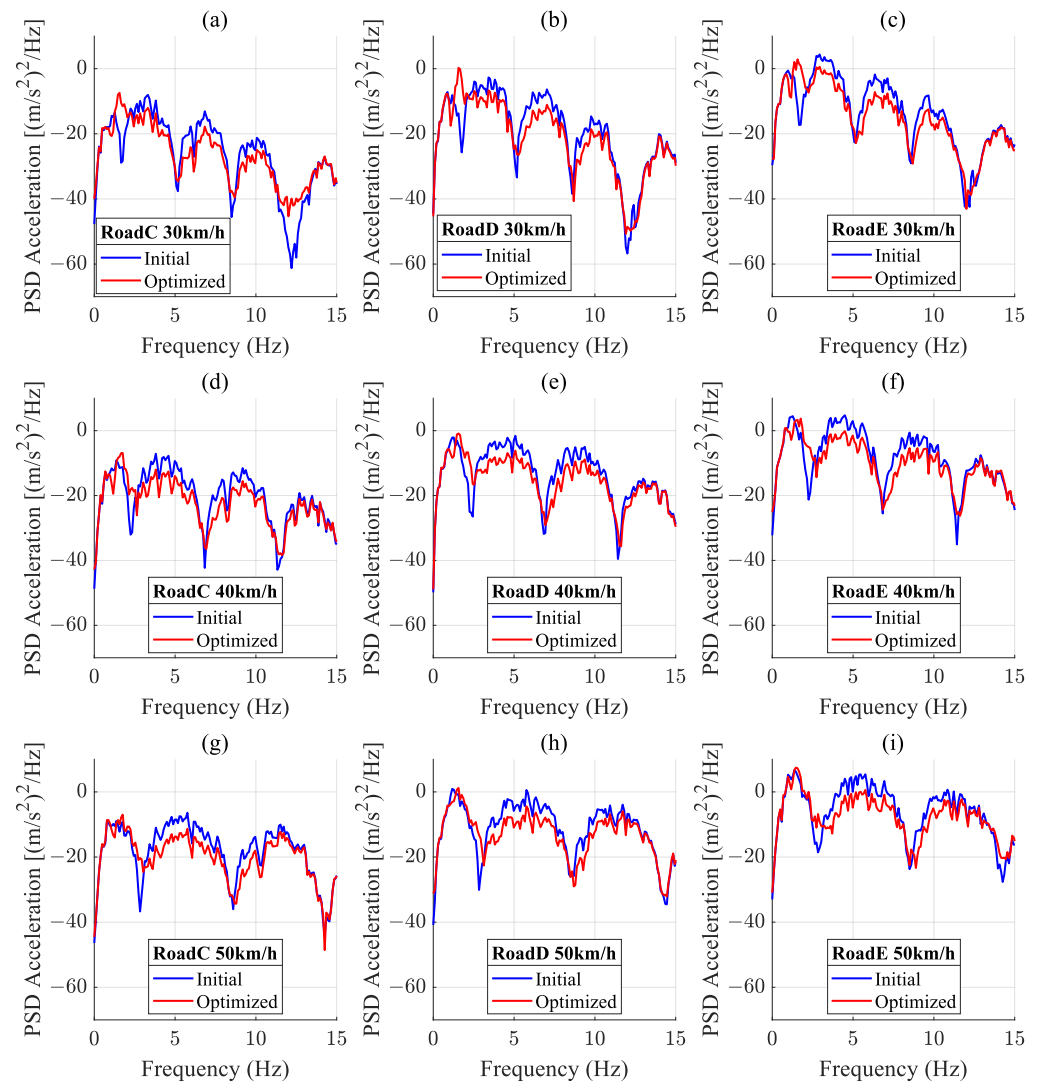
Figure 20. Comparison of power spectral density (PSD) of vertical acceleration for the vehicle body center of mass across different road types and speeds. The optimized configuration (red) achieves consistent reductions in PSD magnitude, particularly in the low- and mid-frequency ranges (0–10 Hz), emphasizing the optimization's effectiveness in reducing vibration and enhancing vehicle comfort.
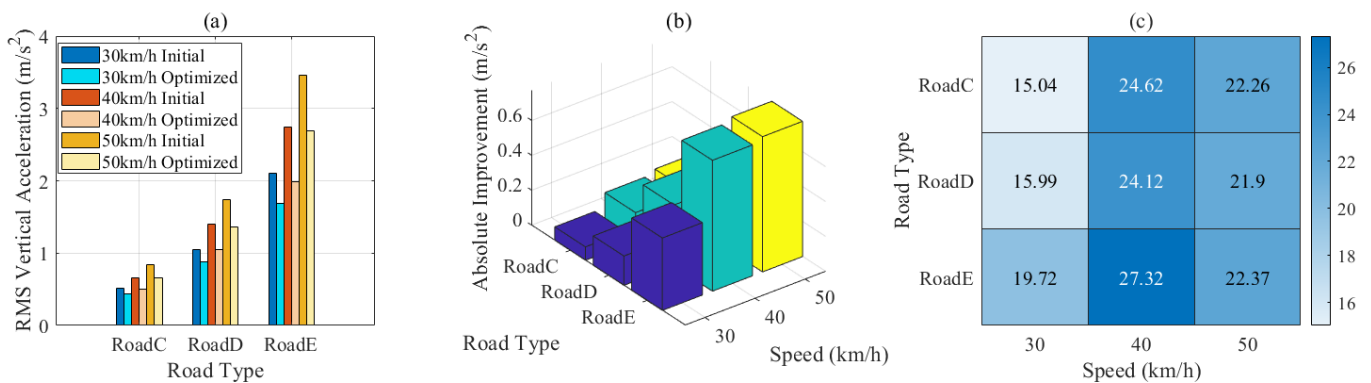
Figure 21. RMS vertical acceleration across different road types (C, D, E) and speeds (30, 40, and 50 km/h). (**a**) Comparison of initial and optimized values. (**b**) Absolute improvements. (**c**) Percentage improvements.

The RMS analysis of front suspension dynamic deflection is carried out in Figure 22. The optimized RMS values were lower than the initial values at all road types and speeds, highlighting the improved suspension travel control. The RMS dynamic deflection im-

provement of all road types is enhanced with increasing speed. The percentage improvement ranged from 19% to 26%, which verifies the robustness of the optimization scheme under complex dynamic conditions, improving the suspension's travel control under different conditions.
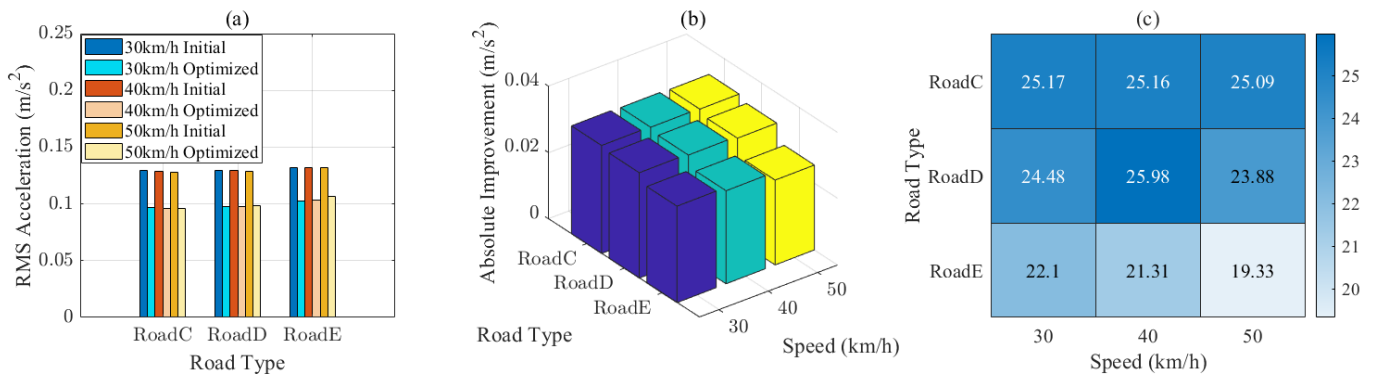
Figure 22. RMS dynamic deflection of the front suspension system across different road types (C, D, E) and speeds (30, 40, and 50 km/h). (**a**) Comparison of initial and optimized values, (**b**) Absolute improvements. (**c**) Percentage improvements.

The RMS analysis of pitch angular acceleration of vehicle centroid is carried out in Figure 23. The RMS value of the optimized is lower than the initial value at most road types and speeds, indicating that the pitch motion of the vehicle decreases significantly. The optimization effect is more obvious on flat roads and at low speeds.
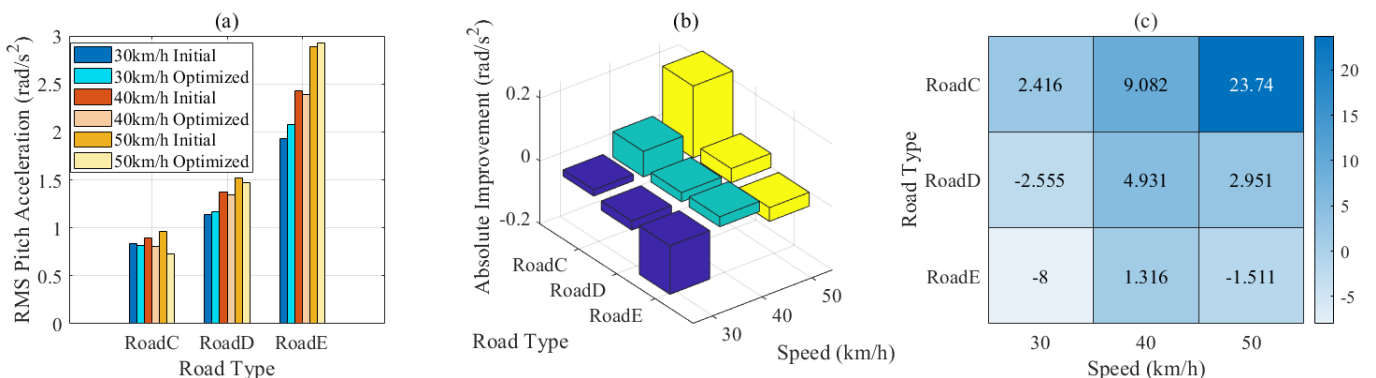
Figure 23. RMS pitch angular acceleration of the vehicle body center of mass across different road types (C, D, E) and speeds (30, 40, and 50 km/h). (**a**) Comparison of initial and optimized values. (**b**) Absolute improvements in pitch angular acceleration. (**c**) Percentage improvements.

6. Discussion

The application of RMSTMM to vehicle system dynamics modeling provides a novel and efficient tool for modeling and analysis and builds a complete modeling, analysis, and performance optimization framework. By combining contact and friction models, the application range of RMSTMM is further extended so that it can more accurately reflect the dynamic behavior of the vehicle under actual working conditions.

In this study, a multi-objective optimization technique is used to obtain a non-inferior solution that performs well under a variety of working conditions, which verifies the effectiveness and robustness of the proposed framework. Frequency and PSD analysis show that the optimization significantly improves vehicle dynamics at different road conditions and speeds, especially in the low and medium frequency ranges, directly improving ride comfort and suspension stability. The percentage of improvement increases with speed,

and the effect is most pronounced on Class E roads, highlighting the adaptability and robustness of the optimization to harsh surfaces. The results demonstrate the effectiveness and scalability of the optimization method in improving ride comfort, reducing vibration, and enhancing suspension performance. The optimization is particularly effective at higher speeds, ensuring better suspension performance in demanding conditions. The optimization significantly reduces the RMS value of pitch acceleration and improves the stability and pitch motion control ability of high-speed driving on flat roads, but the effect on rough road surfaces is limited. It shows that the pitch angle acceleration has a stronger correlation with the road roughness, and the parameter adjustment of the passive suspension has a limited effect. This framework provides an innovative approach to vehicle dynamics research while being highly scalable, enabling more refined dynamics model construction and more advanced optimization methods.

However, the vehicle dynamics model in this study is still relatively simplified, and only the passive suspension is analyzed. The geometry of the suspension is not considered. There is a certain gap between the tire model and the real working condition, and the lack of experimental verification, which are the directions that need to be improved in the follow-up research. In addition, with the rapid development of vehicle intelligence and network technology, vehicle dynamics and performance optimization technology is constantly evolving. The proposed framework has the potential to analyze semi-active suspension and active suspension and provides a solid foundation and research direction for further improving vehicle performance in the future.

7. Conclusions

Using RMSTMM, a novel approach for comprehensive vehicle modeling is introduced. The model accounts for wheel–ground contact and friction and calculates the vehicle's vertical acceleration of the center of mass, dynamic deflection of the front suspension, and angular acceleration of the center of mass while driving at 40 km/h on a Class D road.

Preliminary analysis indicated the need to optimize suspension parameters. Multi-objective Pareto solutions were derived using the NSGA-II algorithm. A representative solution was selected from the Pareto frontier, balancing the competing demands of smoothness, stability, and suspension performance. The vertical acceleration of the center of mass, dynamic deflection of the front suspension, and angular acceleration of the center of mass were reduced by 24.12%, 25.98%, and 4.93%, respectively. The robustness of the optimization results is verified, and the dynamic simulation of Class C, D, and E road conditions is completed at 30 km/h, 40 km/h, and 50 km/h. The frequency, PSD, and RMS analysis were performed at different road conditions and speeds. The optimization results show a significant improvement in dynamic characteristics.

This research highlights the potential of advanced multi-objective optimization techniques in enhancing vehicle dynamics and offers a robust methodology for practical applications. It also extends the use of the transfer matrix method.

Data Availability Statement: The data generated during the current study are available from the corresponding author upon reasonable request.

Conflicts of Interest: The authors declare no conflicts of interest.

Abbreviations

The following abbreviations are used in this manuscript:

CAE	Computer Aided Engineering
MSTMM	Multibody System Transfer Matrix Method
NV-MSTMM	New Version of MSTMM
RMSTMM	Reduced Multibody System Transfer Matrix Method
NSGA-II	Nondominated Sorting Genetic Algorithm II
SPEA2	Strength Pareto Evolutionary Algorithm 2
PESA-II	Pareto Envelope-based Selection Algorithm II
RMS	Root Mean Square
PSD	Power Spectrum Density

References

1. Huang, H.H.; Tsai, M.J. Vehicle Cornering Performance Evaluation and Enhancement Based on CAE and Experimental Analyses. *Appl. Sci.* **2019**, *9*, 5428. https://doi.org/10.3390/app9245428.
2. Jazar, R.N. *Vehicle Dynamics: Theory and Application*; Springer: New York, NY, USA, 2008. https://doi.org/10.1007/978-0-387-74244-1.
3. Viadero-Monasterio, F.; Boada, B.L.; Zhang, H.; Boada, M.J.L. Integral-based event triggering actuator fault-tolerant control for an active suspension system under a networked communication scheme. *IEEE Trans. Veh. Technol.* **2023**, *72*, 13848–13860. https://doi.org/10.1109/TVT.2023.3279460.
4. Viadero-Monasterio, F.; Meléndez-Useros, M.; Jiménez-Salas, M.; Boada, B.L. Robust Static Output Feedback Control of a Semi-Active Vehicle Suspension Based on Magnetorheological Dampers. *Appl. Sci.* **2024**, *14*, 10336. https://doi.org/10.3390/app142210336.
5. Viadero-Monasterio, F.; Boada, B.; Boada, M.; Díaz, V. H_∞ dynamic output feedback control for a networked control active suspension system under actuator faults. *Mech. Syst. Signal Process.* **2022**, *162*, 108050. https://doi.org/10.1016/j.ymssp.2021.108050.
6. Liang, J.; Lu, Y.; Pi, D.; Yin, G.; Zhuang, W.; Wang, F.; Feng, J.; Zhou, C. A Decentralized Cooperative Control Framework for Active Steering and Active Suspension: Multi-Agent Approach. *IEEE Trans. Transp. Electrif.* **2022**, *8*, 1414–1429. https://doi.org/10.1109/TTE.2021.3096992.
7. Azmi, R.; Mirzaei, M.; Habibzadeh-Sharif, A. A novel optimal control strategy for regenerative active suspension system to enhance energy harvesting. *Energy Convers. Manag.* **2023**, *291*, 117277. https://doi.org/10.1016/j.enconman.2023.117277.
8. Shaqarin, T.; Noack, B.R. Enhancing Mechanical Safety in Suspension Systems: Harnessing Control Lyapunov and Barrier Functions for Nonlinear Quarter Car Model via Quadratic Programs. *Appl. Sci.* **2024**, *14*, 3140. https://doi.org/10.3390/app14083140.
9. Feng, J.; Liang, J.; Lu, Y.; Zhuang, W.; Pi, D.; Yin, G.; Xu, L.; Peng, P.; Zhou, C. An Integrated Control Framework for Torque Vectoring and Active Suspension System. *Chin. J. Mech. Eng.* **2024**, *37*, 10. https://doi.org/10.1186/s10033-024-00999-6.
10. Karim Afshar, K.; Korzeniowski, R.; Konieczny, J. Evaluation of Ride Performance of Active Inerter-Based Vehicle Suspension System with Parameter Uncertainties and Input Constraint via Robust H_∞ Control. *Energies* **2023**, *16*, 4099. https://doi.org/10.3390/en16104099.
11. Ferhath, A.A.; Kasi, K. The evolution of damper technology for enhanced ride comfort and vehicle handling in vehicle suspension system. *Int. J. Dyn. Control* **2024**, *12*, 3908–3946. https://doi.org/10.1007/s40435-024-01489-2.
12. Zhang, J.; Liu, Z.; Qin, Z. Passive Suspension Design and Dynamics Analysis of Manned Lunar Rover. In Proceedings of the 2024 10th International Conference on Mechatronics and Robotics Engineering (ICMRE), Milan, Italy, 27–29 February 2024; pp. 155–160. https://doi.org/10.1109/ICMRE60776.2024.10532165.
13. Gobbi, M.; Levi, F.; Mastinu, G. Multi-objective stochastic optimisation of the suspension system of road vehicles. *J. Sound Vib.* **2006**, *298*, 1055–1072. https://doi.org/10.1016/j.jsv.2006.06.041.
14. Lenka, V.R.; Anthonysamy, B.; Londhe, A.; Hatekar, H. *Multi-Objective Optimization to Improve SUV Ride Performances Using MSC. ADAMS and Mode Frontier*; SAE Technical Paper Series; SAE: Warrendale, PA, USA, 2008. https://doi.org/10.4271/2018-01-0575.
15. Su, Z.; Xu, F.; Hua, L.; Chen, H.; Wu, K.; Zhang, S. Design optimization of minivan MacPherson-strut suspension system based on weighting combination method and neighborhood cultivation genetic algorithm. *Proc. Inst. Mech. Eng. Part D J. Automob. Eng.* **2019**, *233*, 650–660. https://doi.org/10.1177/0954407018789303.

16. Ebrahimi-Nejad, S.; Kheybari, M.; Borujerd, S.V.N. Multi-objective optimization of a sports car suspension system using simplified quarter-car models. *Mech. Ind.* **2020**, *21*, 412. https://doi.org/10.1051/meca/2020039.

17. Issa, M.; Samn, A. Passive vehicle suspension system optimization using Harris Hawk Optimization algorithm. *Math. Comput. Simul.* **2022**, *191*, 328–345. https://doi.org/10.1016/j.matcom.2021.08.016.

18. Schiehlen, W.; Others. *Multibody Systems Handbook*; Springer: Berlin/Heidelberg, Germany, 1990; Volume 6.

19. Shabana, A.A. *Dynamics of Multibody Systems*; Cambridge University Press: Cambridge, UK, 2020.

20. Rui, X.; Zhang, J.; Wang, X.; Rong, B.; He, B.; Jin, Z. Multibody system transfer matrix method: The past, the present, and the future. *Int. J. Mech. Syst. Dyn.* **2022**, *2*, 3–26. https://doi.org/10.1002/msd2.12037.

21. Pestel, E.C.; Leckie, F.A.; Kurtz, E.F. Matrix methods in elastomechanics. *J. Appl. Mech.* **1964**, *31*, 574.

22. Rui, X.; Bestle, D.; Zhang, J.; Zhou, Q. A new version of transfer matrix method for multibody systems. *Multibody Syst. Dyn.* **2016**, *38*, 137–156. https://doi.org/10.1007/s11044-016-9528-5.

23. Rui, X.; Bestle, D. Reduced multibody system transfer matrix method using decoupled hinge equations. *Int. J. Mech. Syst. Dyn.* **2021**, *1*, 182–193. https://doi.org/10.1002/msd2.12026.

24. Chen, D.; Gu, C.; Marzocca, P.; Yang, J.; Pan, G. Dynamic modeling of rotating blades system based on transfer matrix method of multibody system. *Appl. Math. Model.* **2022**, *105*, 475–495. https://doi.org/10.1016/j.apm.2021.12.039.

25. Si, G.; Li, W.; Lu, H.; Zhang, Z.; Zhang, X. Vibration Modeling and Analysis of a Flexible 3-PRR Planar Parallel Manipulator Based on Transfer Matrix Method for Multibody System. *Machines* **2023**, *11*, 505. https://doi.org/10.3390/machines11050505.

26. Chen, W.; Du, C.; Liu, F.; Men, Y.; Zhang, X.; Li, B. Dynamics modeling and impact response of a rescue robot with two flexible manipulators. *J. Braz. Soc. Mech. Sci. Eng.* **2024**, *46*, 217. https://doi.org/10.1007/s40430-024-04794-1.

27. Li, B.; Zhao, W.; Miao, Y.; Tian, W.; Liao, W. A method for dynamic parameter identification of an industrial robot based on frequency response function. *Int. J. Mech. Syst. Dyn.* **2024**, *4*, 461–471. https://doi.org/10.1002/msd2.12131.

28. Miao, Y.; Tian, W.; Liao, W.; Duan, J.; Ye, J. Collision dynamics modelling and testing of compliant buffering adsorption system under microgravity environment. *Nonlinear Dyn.* **2024**, *112*, 13785–13801. https://doi.org/10.1007/s11071-024-09773-8.

29. Miao, Y.; Rui, X.; Wang, P.; Zhu, H.; Zhang, J.; Wang, J. Nonlinear dynamic modeling and analysis of magnetorheological semi-active suspension for tracked vehicles. *Appl. Math. Model.* **2024**, *125*, 311–333. https://doi.org/10.1016/j.apm.2023.09.027.

30. Wu, G.; Rui, X.; Wang, G.; Jiang, M.; Wang, X. Modelling and simulation of driving dynamics of wheeled launch system under random road surface excitation. *Acta Mech. Sin.* **2024**, *40*, 523310. https://doi.org/10.1007/s10409-023-23310-x.

31. Deb, K.; Pratap, A.; Agarwal, S.; Meyarivan, T. A fast and elitist multiobjective genetic algorithm: NSGA-II. *IEEE Trans. Evol. Comput.* **2002**, *6*, 182–197. https://doi.org/10.1109/4235.996017.

32. Gadhvi, B.; Savsani, V.; Patel, V. Multi-Objective Optimization of Vehicle Passive Suspension System Using NSGA-II, SPEA2 and PESA-II. *Procedia Technol.* **2016**, *23*, 361–368. https://doi.org/10.1016/j.protcy.2016.03.038.

33. Nagarkar, M.P.; Vikhe Patil, G.J.; Zaware Patil, R.N. Optimization of nonlinear quarter car suspension-seat-driver model. *J. Adv. Res.* **2016**, *7*, 991–1007. https://doi.org/10.1016/j.jare.2016.04.003.

34. Fossati, G.G.; Miguel, L.F.F.; Casas, W.J.P. Multi-objective optimization of the suspension system parameters of a full vehicle model. *Optim. Eng.* **2019**, *20*, 151–177. https://doi.org/10.1007/s11081-018-9403-8.

35. Nandihal, P.V.; Mohan, A.; Saha, S.K. *Dynamics of Rigid-Flexible Robots and Multibody Systems*; Springer Singapore Pte. Limited: Singapore, 2021.

36. Wittenburg, J. *Dynamics of Systems of Rigid Bodies*; B. G. Teubner: Stuttgart, Germany, 1977; Volume 33.

37. Brandl, H.; Johanni, R.; Otter, M. An Algorithm for the Simulation of Multibody Systems with Kinematic Loops. In Proceedings of the IFToMM Seventh World Congress on the Theory of Machines and Mechanisms, Seville, Spain, 17–22 September 1987.

38. Marques, F.; Flores, P.; Lankarani, H.M., On the Frictional Contacts in Multibody System Dynamics. In *Multibody Dynamics: Computational Methods and Applications*; Springer International Publishing: Cham, Swizterland, 2016; pp. 67–91. https://doi.org/10.1007/978-3-319-30614-8_4.

39. Qin, Y.; Wang, Z.; Xiang, C.; Hashemi, E.; Khajepour, A.; Huang, Y. Speed independent road classification strategy based on vehicle response: Theory and experimental validation. *Mech. Syst. Signal Process.* **2019**, *117*, 653–666. https://doi.org/10.1016/j.ymssp.2018.07.035.